2015

Improvement of Transient Stability of Photovoltaic-hydro Microgrids Using Virtual Synchronous Machines

Ujjwol Tamraker
South Dakota State University

IMPROVEMENT OF TRANSIENT STABILITY OF PHOTOVOLTAIC-HYDRO MICROGRIDS USING VIRTUAL SYNCHRONOUS MACHINES

BY

UJJWOL TAMRAKAR

A thesis submitted in partial fulfillment of the requirements for the

Master of Science

Major in Electrical Engineering

South Dakota State University

2015

IMPROVEMENT OF TRANSIENT STABILITY OF PHOTOVOLTAIC-HYDRO MICROGRIDS USING VIRTUAL SYNCHRONOUS MACHINES

This thesis is approved as a creditable and independent investigation by a candidate for the Master of Science in Electrical Engineering degree and is acceptable for meeting the thesis requirements for this degree. Acceptance of this thesis does not imply that the conclusions reached by the candidate are necessarily the conclusions of the major department.

Dr Reinaldo Tonkoski,
Major/Thesis Advisor Date

Dr David Galipeau,
Thesis Advisor Date

Dr. Steven Hietpas Date
Head, Electrical Engineering and Computer Science

Dean, Graduate School Date

ACKNOWLEDGMENTS

I would like to express my sincere gratitude towards my research advisor Dr. Reinaldo Tonkoski for his crucial advice and sharing his profound knowledge and believing in me from the very beginning of the thesis research. Without his persistent support and guidance throughout the various stages of the study, it would not have come out in such an ease. I would like to take this opportunity to appreciate Dr. David Galipeau for the valuable advice and for providing necessary information and guidance to carry out the research. Moreover, I would like to thank Dr. Wei Sun for being in my committee and reviewing my work.

I am very much thankful to South Dakota State University, Department of Electrical Engineering & Computer Science for providing me the necessary resources for this research work.

I am thankful to my father Dr. Indraman Tamrakar, for being my mentor in my study along with my mother Pabitra Tamrakar and sister Elisha Tamrakar for providing me unconditional love, support and motivation. Also I owe my special thanks Jharna Pokhrel for providing encouragement and support every day.

Last but not least, my everlasting gratitude goes to all my friends and all the people in South Dakota State University, who helped me for out this research and made my study a fulfilling and memorable one.

CONTENTS

ABBREVIATIONS

AC	Alternating Current
BJT	Bipolar Junction Transistor
DC	Direct Current
DQ	Direct – Quadrature Axis
IEEE	Institute of Electrical and Electronics Engineers
IGBT	Insulated Gate Bipolar Transistor
MATLAB	Matrix Laboratory
MOSFET	Metal Oxide Semiconductor Field Effect Transistor
MPPT	Maximum Power Point Tracking
PID	Proportional Integral Derivative
PLL	Phase Locked Loop
PV	Photovoltaic
ROCOF	Rate of Change of Frequency
SPWM	Sinusoidal Pulse Width Modulation
SOC	State of Charge
VSM	Virtual Synchronous Machine

LIST OF FIGURES

LIST OF TABLES

ABSTRACT

IMPROVEMENT OF TRANSIENT STABILITY OF PHOTOVOLTAIC-HYDRO MICROGRIDS USING VIRTUAL SYNCHRONOUS MACHINES

UJJWOL TAMRAKAR

2015

Photovoltaic-hydro microgrids can provide reliable clean energy in remote areas that do not have an electric grid. Higher photovoltaic penetration can cause large frequency deviations at a high rate of change of frequency in the system. Virtual synchronous machines have been used to enhance performance of a diesel hybrid mini-grid but no studies have been performed to account for dynamics of a hydro system. A method is needed to improve the transient stability of photovoltaic-hydro microgrid systems while allowing high photovoltaic penetration. The objective of this thesis was to study the feasibility of using virtual synchronous machines to improve transient stability of photovoltaic-hydro microgrid systems. A virtual synchronous machine is a short term energy storage device with power electronics and a dispatching algorithm that provides inertia to the grid. Transient analysis of a 25 kWp-39 kW photovoltaic–hydro benchmark system was performed using a MATLAB\Simulink simulation with and without the virtual synchronous machine. The virtual synchronous machine was modeled using direct-quadrature axis based current control techniques, and software in the loop simulations were performed in Opal-RT real time digital simulator. Large frequency deviations and rate of change of frequency were observed when the virtual synchronous machine was not included. When the virtual synchronous machine was used, frequency deviations and the rate of change of frequency were reduced to within limits. The energy use was minimal

and comparable to small lead acid or NiMH batteries. Hence, virtual synchronous machines can improve the transient stability of photovoltaic-hydro systems while allowing high photovoltaic penetration.

CHAPTER 1 INTRODUCTION

1.1. Background

Environmental concerns and fast rising cost of traditional fossil fuel based energy sources have encouraged the growth of renewable energy based energy sources in recent times. Hybrid microgrid systems consisting of sources like diesel/natural gas generators, hydro, biomass generators, wind and photovoltaic (PV) generations are gaining popularity. The flexibility of such hybrid microgrid systems to operate in the isolated and grid connected mode is one of the main factors behind the rapid growth of such systems. The exponential drop in the cost of the PV systems has been a contributing a factor for its widespread use. PV and hydro systems complement each other, especially in regions where there are distinct wet and dry seasons. However, the intermittent nature of photovoltaic generation raises many issues that need to be addressed.

Reliable remote microgrids are essential for consumers and incoming generating processes in rural areas of the world like Nepal where 44% of the people still live without electricity. PV only microgrids are unreliable due to the intermittent nature of solar energy. Furthermore, at night PV systems cannot provide electricity unless some kind of energy storage is used. Various energy storage technologies are available today including batteries, compressed air storage and flywheels to deal with this stochastic nature of photovoltaic generation. Batteries are the most commonly used storage elements in PV systems. However batteries are expensive and can be hazardous. Hydro systems can complement PV systems as a viable renewable means of energy storage. PV-hydro hybrid microgrids can provide reliable clean energy in the remote areas where the electricity grid

has not been extended. With such hybrid PV-hydro systems there is a possibility of interconnection between many such isolated systems to form a mini-grid and eventually when the grid does expand to these remote regions, provide support to the grid. The penetration of PV into hydro systems is however limited by many factors [1]. With addition of PV into the hydro systems, the overall inertia of the system decreases since PV does not store energy. Conventionally, the large mass of synchronous generators provide inertia to the system which is critical for the stability of such systems, but PV has no inertia. Hence, the inertia of PV–hydro based microgrid systems is limited to that from the hydro system.

Decreased inertia is problematic in isolated PV–hydro microgrid systems. In the isolated mode of operation from the grid, the hydro system controls the frequency of the system (i.e., isochronous mode of operation) and typically cannot handle the fast frequency dynamics introduced by the PV system. This problem becomes even more prominent when the PV irradiance is highly varying. So, the transient stability of PV–hydro microgrids systems operating in isolated mode is poor. Load changes, generation changes and large PV fluctuations can cause large frequency deviations at a large rate of change of frequency (ROCOF). This causes the frequency sensitive relays to be triggered cutting off even more load or generations which leads to a further mismatch between generation and loads in the system. This may lead to cascaded outages and a complete system failure. Battery based energy storage systems have been used to assist in the frequency regulation of the system through the primary frequency control. But the primary control acts only after a few seconds of a frequency disturbance and releases/absorbs power based on a pre-defined droop characteristics [2]. If the initial rate of change of

frequency following a disturbance is very high, the primary frequency control cannot act fast enough and large frequency deviations occur in a very short time in the system causing instability [3]. Hence, a dynamic frequency control is required which acts much faster than the primary frequency control (within a few milliseconds) so that it can reduce the high initial rate of change of frequency and keep the system stable.

A virtual synchronous machine is one such short term energy storage device with power electronics and a dispatching algorithm which makes it behave like a synchronous generator to grid [4]. It emulates the inertial and damping properties of a real synchronous generator by adding these properties and takes part in the initial inertial response of the system much like a conventional synchronous generator does.

1.2. Previous Work

The feasibility of integration of photovoltaic energy into existing hydroelectric plants was studied by Margeta et.al. in 2011. They found that the price of electrical energy from this hybrid system was competitive with other renewable energy sources but still expensive compared to the conventional sources [5]. Turkay et.al. in 2011 presented an economic analysis to show that renewable energy sources would need to be oversized to make them completely reliable which could further increase cost of such systems. However, they found that integration of renewables sources such as solar and wind to form a hybrid generation system reduced the fluctuations and reduced energy storage requirements. They further concluded that a hybrid electric generation system consisting of the grid, solar and hydroelectric generation was the most feasible solution from an economic point of view [6]. Zhao et.al. in 2011 showed that the intermittent nature of photovoltaic generation limited its use and led to undesired system performance [7].

Gurung et.al. in 2013 found that only 45% photovoltaic penetration can be achieved if the frequency has to be within normal operating frequency range of (± 2%) with system inertia constant of 5 seconds. The penetration was found to reduce dramatically with decreased system inertia constants. They concluded that higher system inertia is required to achieve higher photovoltaic penetration levels [1].

Tielens et.al in 2012 showed that due to the intermittent nature of renewable sources, they are not able to provide any frequency control nor add to the total system inertia [8]. Ulbig et.al. in 2014 showed that the traditional concept of the grid having an infinite amount of inertia is no longer true for modern power systems with a high percent of renewable energy generation. The fast dynamics introduced by renewable sources required better control systems for stable system operation [9]. The frequency variations in autonomous power system consisting of two 26 kW diesel generators and 20 kW fixed speed wind generator was studied by Torres et.al. in 2011. They found that such systems were inclined to frequency variations due to shortage of inertia and power reserves. Disturbances in these systems can severely affect the transient stability of the system [10].

Beltran et.al. in 2013 analyzed the use of energy storage systems to reduce the intermittent nature of photovoltaic generations and produce constant power from a photovoltaic plant. The energy storage requirements were found to be very high and not economically viable [11]. Lazarewicz et.al in 2012 reported the use of various energy storage technologies in microgrids. Flywheels and capacitors were proposed for small cycle usage whereas batteries and pumped hydro were proposed for long cycle usage. A hybrid solution containing a mixture of energy storage from different domains was also suggested [12]. Pena-Alzola in 2011 showed the use of flywheel based energy storage

systems to compensate power fluctuations due to renewable generation sources. Flywheel based energy storage is used when a large number of charging and discharging cycles are required in a period of seconds. But constant maintenance was one of the main drawbacks of flywheel based energy storage systems [13]. Espinar et.al. in a comprehensive study found that energy storage can play a significant role in stabilization of microgrids. Four storage technologies were recommended for microgrid stabilization, lead acid batteries, super-capacitors, Li-ion batteries and flywheels because of their response time and power density. However, they found that lead acid batteries had to be oversized to meet power demand. Super-capacitors were found be the most suitable option but its use is still limited by the cost [14]. Energy storage systems used for primary frequency regulation purposes has been shown in [2, 15, 16] but the impact of high rate of change of frequency with the addition of large number of renewable generation has not been analyzed.

The dependence of microgrids on the larger rotational mass of synchronous generators for system inertia was shown by Tielens et.al in 2012. Higher renewable penetration caused large frequency deviations at a high rate of change of frequency (ROCOF) which could not be handled by conventional governor control of the synchronous generators [8]. The concept of virtual synchronous machines (VSM) to emulate inertia through the use of power electronics converters was first proposed by Beck et. al in 2007 [17] . In another study Hesse et.al in 2009 used VSM implemented using a hysteresis current controlled inverter for microgrid stabilization. The system ran a direct-quadrature (DQ) frame based model of a synchronous machine in a digital signal processor to emulate the characteristics of a synchronous generator [18]. Visscher et.al. in 2008 proposed a control scheme for VSM based on a dynamic model of a synchronous

generator. This allowed for easier control over emulated inertia and damping effect by simple modification of parameters in the model. The possibility of using VSM during the islanding of microgrids was also introduced [19]. A different approach for implementation of VSMs by modeling the swing equation of a synchronous generator was presented by Sakimoto et.al. in 2011 [20]. In a simulation Soni et.al in 2013 showed that virtual inertia can also emulated by modifying the droop gains of the existing inverters based on the system ROCOF. This method reduced the amount of storage required for microgrids with high renewable energy share [21]. In a real time simulation, Karapanos et.al. in 2011 showed that with addition of VSM the frequency deviations in the system was reduced by 35% [22]. VSM was used to improve dynamic frequency control of an autonomous power system consisting of diesel generators and wind systems by Torres et.al in 2013. A technique to optimize the virtual inertia required to keep the system stable was also developed [23].

No study has been found on application of VSMs to stabilize PV – hydro microgrid systems. The literature also lacks the analysis on potential of increasing PV penetration in microgrids using the concept of the VSM.

1.3. Motivation

Need a method to improve transient stability for PV–hydro microgrid systems allowing higher level of PV penetration. The hypothesis for this study is that if inertia is added to the PV-hydro microgrid system using a VSM it will maintain and may even improve its transient stability.

1.4. Objective

The objective of this thesis was to study the feasibility of using virtual synchronous machines to improve transient stability of PV-hydro microgrid systems. The specific tasks of this research were to:

1. Study transient stability of PV–hydro microgrid systems.
2. Study and analyze the use of virtual synchronous machines to reduce frequency variations in PV–hydro microgrid system and improve its transient stability.
3. Analyze energy storage requirements for implementation of virtual synchronous machine.

The tasks performed will indicate the energy storage and the peak power requirements of the VSM to increase the penetration levels in PV-hydro microgrids while maintaining its transient stability. Furthermore, the study will also provide methods to determine additional inertia requirements to keep PV-hydro microgrid system stable.

1.5. Thesis Outline

This thesis has been organized as follows: Chapter 2 defines the concept of transient stability of a power system in general including that of a PV-hydro microgrid system and the concept of virtual synchronous machines. Chapter 3 introduces the transient stability analysis procedures, design of the virtual synchronous machine and software in the loop simulations in Opal-RT real time digital simulator. Chapter 4 presents the simulation results and analysis. Finally, chapter 5 presents the conclusions, limitations and possible future work.

CHAPTER 2 THEORY

Chapter 2 introduces PV-hydro microgrids and discusses the transient stability of PV-hydro microgrid systems. The modeling and control of three phase voltage source inverters using direct-quadrature axis (DQ) theory is described followed by the theory behind virtual synchronous machines and its operating principle.

2.1. Photovoltaic hydro microgrid systems

A photovoltaic (PV) hydro microgrid is a hybrid system consisting of a hydro generator and a PV system. The PV system provides energy to the load demand when energy is available from the sun. The deficit energy is provided by the hydro system. In case of pumped hydro systems, water can thus be stored for use at times when PV is not available or in some cases for other socio-economic activities such as irrigation.

2.1.1. Hydro systems

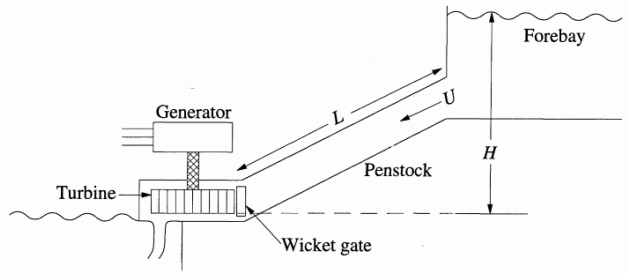

Figure 2.1. A typical hydro system and its components [24].

A hydro system is a renewable source of electric generation which converts the potential and kinetic energy of the water into electrical energy. Figure 2.1 shows the basic components of a typical hydro system. The water stored in the reservoir (Forebay) is taken in from the intake and allowed to pass through the penstock. The water then strikes the

turbine after passing through the wicket gate which in turn rotates the turbine. The rotating turbine is mechanically coupled with shaft of the generator. Thus, the generator converts the rotational motion into electrical energy which is then delivered to the consumers through the power lines. The mechanical power intake into the turbine is controlled by a governor with the wicket gate. The water after passing through the turbine is allowed to flow into the tailrace.

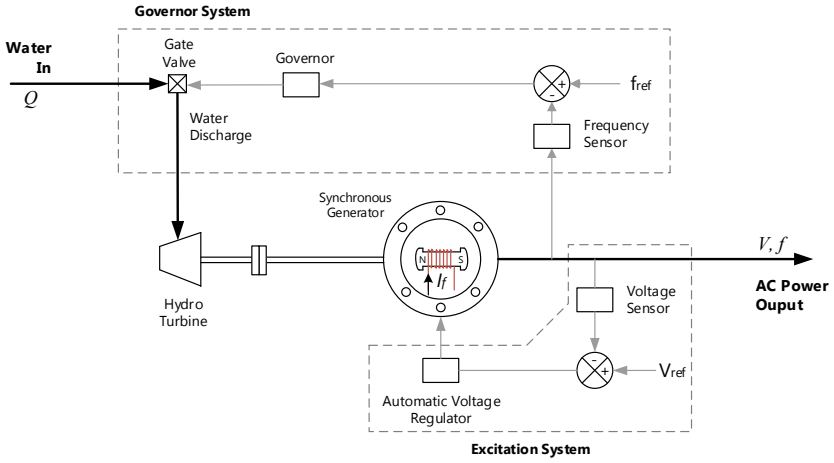

Figure 2.2. Detailed diagram of the hydro system with governor and excitation system.

Figure 2.2 shows a more detailed diagram of the hydro system. The three phase synchronous generator is the main core of the hydro system. The three phase generator converts the mechanical power input from the rotating hydro turbine into electrical power based on Faraday's laws of electromagnetic induction. The governor and excitation systems control the frequency and the magnitude voltage of generated electric power respectively. A frequency sensor is used to sense the frequency of the generated voltage which is then compared with the reference frequency, $f_{ref,}$ and the error signal so obtained is used to drive the governor. The governor then controls the gate valve opening to either increase or decrease the water flow into the turbine. Thus by controlling the water flow

into the turbine and consequently its speed of rotation, the speed of the synchronous generator and the frequency of the electric power produced can be controlled. Similarly, a voltage sensor is used to sense the magnitude of the output voltage of the generator. This voltage is then compared with the reference voltage, V_{ref}, and the error signal drives the voltage regulator. The voltage regulator then controls the field winding current, I_f, which in turn controls the magnitude of the output voltage of the synchronous generator.

1. Governor system for frequency control

Whenever there is a disturbance in the hydro system, like a sudden load change or a short circuit of generator terminals or load terminals for a few milliseconds the frequency of hydro system is disturbed from its steady state value. This is due to the inherent relationship between active power and frequency in hydro systems that relates the frequency to the active power [22]. In such a case, a closed loop control system is required to bring the frequency of the system to back steady state value again. This closed loop system which maintains the system frequency at the rated value is known as the governor system. The hydro systems can have two types of governors:

(a) Isochronous / Constant speed governor

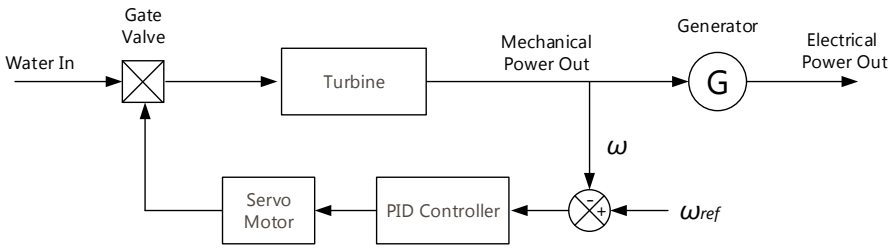

Figure 2.3. Details of an isochronous governor.

Figure 2.3 shows an isochronous governor with a PID (Proportional-Integral-Derivate) based controller. An isochronous governor adjusts the turbine gate–valve to bring the system frequency back to the reference value whenever there is a disturbance and the system the frequency changes. The measured frequency ω is compared with the reference frequency ω_{ref} and based on the error the PID controller then adjusts the gate valve opening to either increase or decrease the input mechanical power with the servo motor so that it matches the electrical output power.

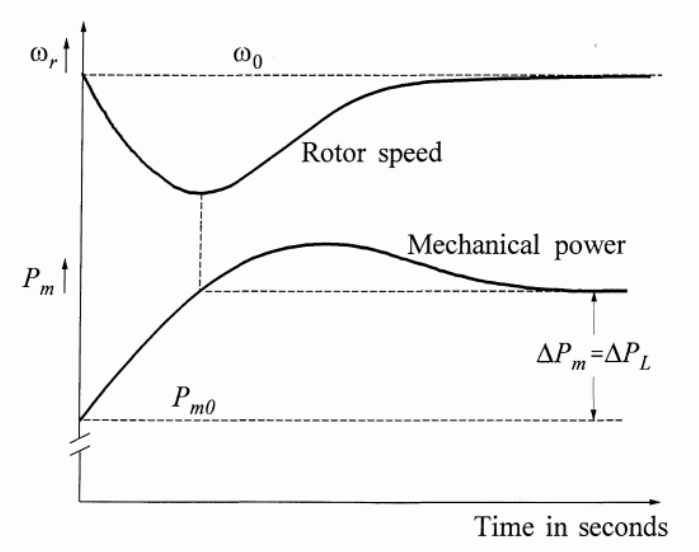

Figure 2.4. Rotor frequency and mechanical power response of generating unit with isochronous governor [24].

Figure 2.4 shows the typical frequency response of a hydro unit after a load increase of ΔP_L. The increase in load causes the frequency to drop below the rated frequency of ω_0. As the speed and frequency drops, the governor increases the mechanical input power, this reduces the rate of frequency drop. When the mechanical power starts exceeding the electrical power demand, the

speed of the rotor / turbine increases and the frequency reaches the rated value of ω. The increase in mechanical power ΔP_m is equal to the electrical load change at this point.

(b) Governor with droop characteristics

Isochronous governors are only applicable in isolated systems with only one generator. But in a system with multiple generators, the isochronous governor cannot bring the system frequency back to a steady value. Hence, a speed regulation or droop characteristic needs to be added to the isochronous governors in each generating unit so that each generators responds to system disturbance based on the set droop value. This can be achieved by adding a feedback loop around the PID controller as shown in Figure 2.5.

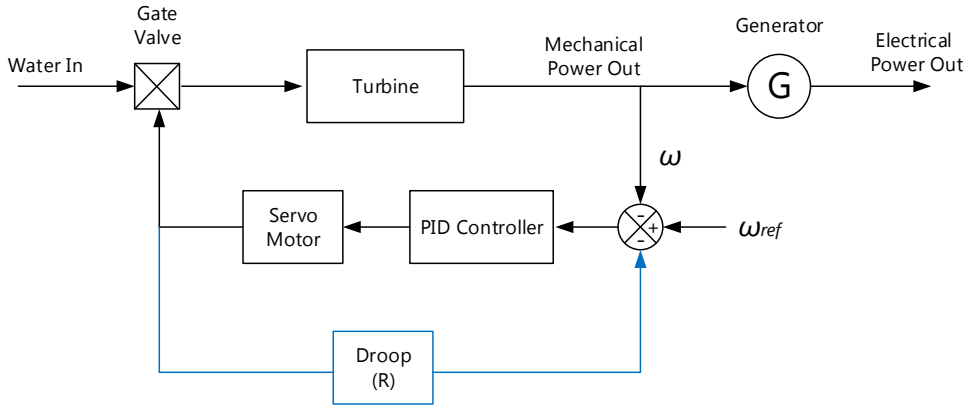

Figure 2.5. Details of a governor with speed droop characteristics.

2. Excitation system for voltage control

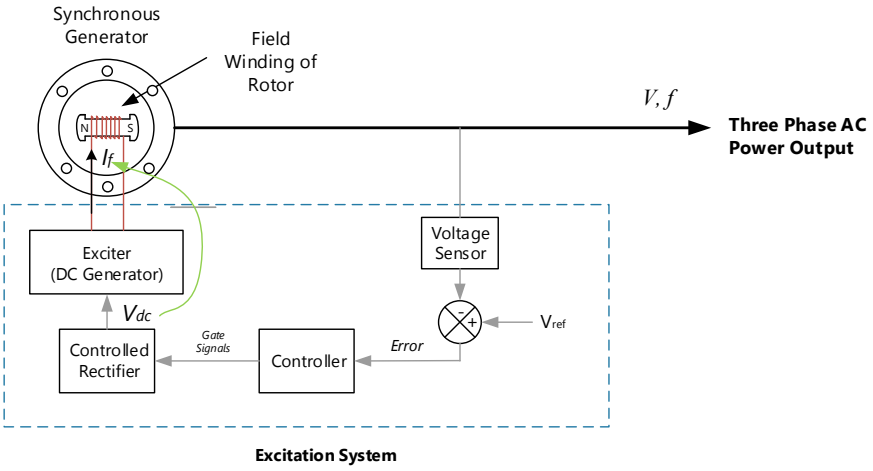

Figure 2.6. Details of an excitation system.

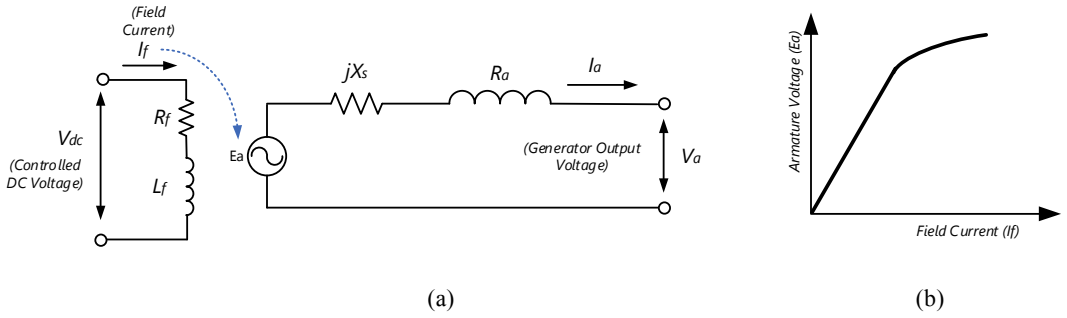

Figure 2.7. (a) Equivalent circuit of synchronous machine. (b) Armature voltage of synchronous machine vs field winding current.

The excitation system is used initially to magnetize the rotor of synchronous generator with the exciter as shown in Figure 2.6. When the generator of the hydro system starts generating power the excitation maintains the system voltage against variations caused by any disturbance. The voltage sensor senses the magnitude of the output voltage of the system and compares it with the reference voltage V_{ref}. The error signal then drives the controller which in turn generates the gate signals for the controlled rectifier. The

controlled rectifier produces a variable DC voltage V_{dc} based on the gate signals. This voltage then excites the DC generator which produces a proportional field current I_f as shown in Figure 2.7 (a). The voltage produced by the generator E_a depends upon the magnitude of the field current as shown in Figure 2.7 (b). The voltage magnitude of the synchronous generator V_a thus varies based on the magnitude of the field current I_f.

2.1.2. PV systems

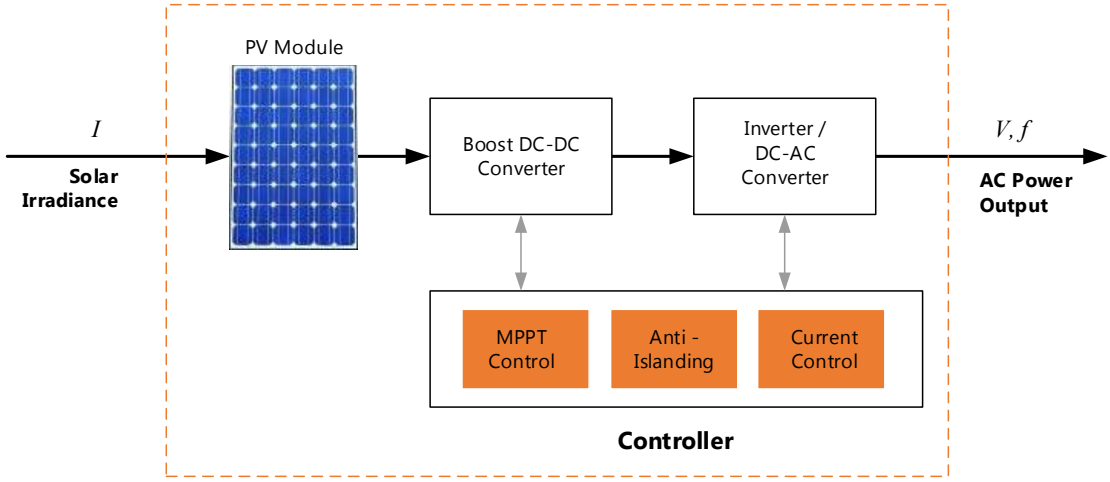

Figure 2.8. Details of a grid connected PV system.

A grid tied PV system as shown Figure 2.8 consists of PV module(s) which is connected to a DC-DC boost converter. The PV module(s) converts the input solar irradiance I to electrical energy output. The DC-DC converter then steps up the input voltage from the PV module to a higher DC voltage required for the inverter. The inverter finally converts the DC power from the PV modules to AC power which can be connected to the grid. The inverter is typically connected to the grid as a current source that feeds current into the grid with the grid creating the voltage source. All the energy conversions are controlled by a controller which performs various controls like MPPT (Maximum

Power Point Tracking) control, current control for the inverter and provides features like anti-islanding among others. Anti-islanding is a feature mandated by the IEEE 1547 standard for grid connected PV inverters according to which if the grid goes down (due to a voltage or frequency disturbance) the inverter output to the grid must shutdown within 2 seconds. Upon restoration of the grid the inverter must monitor the voltage and frequency for 5 minutes to check if the voltage and frequency are within the prescribed limits [25].

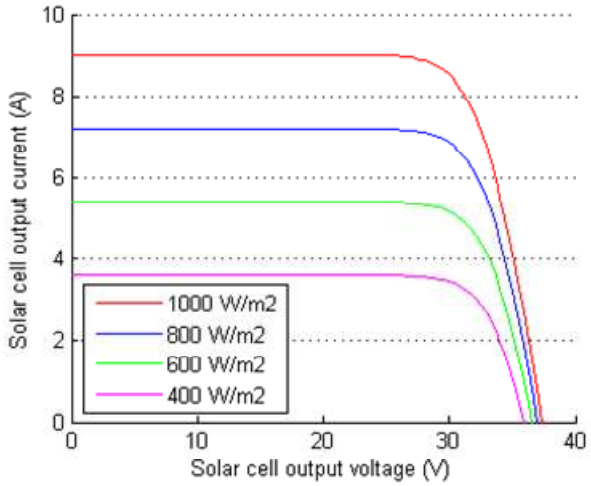

Figure 2.9. IV curve of a PV module at different irradiance levels [26].

The PV modules are made up of semiconductor devices known as solar cells. The photons from the sunlight are absorbed by these solar cells which in turn release electrons resulting in flow of current when a load is connected to its terminals. The current generated by the photovoltaic modules depends on the incident solar irradiance intensity. The I-V curve of a typical PV module is shown in Figure 2.9 which shows the dependence of current generated on the available solar irradiance. With increase in the solar irradiance the current output from the PV modules also increases proportionately. In the ideal case, the current, I, versus the voltage, V, is given by [25]

$$I = I_l - I_0(e^{\frac{qV}{KT}} - 1) \quad (2.1)$$

where, I_l is the component of the cell current due to photons, I_0 is the saturation current, $q = 1.6 \times 10^{-19}$C and $K = 1.38 \times 10^{-23}$ J/K and T is the cell temperature in kelvin.

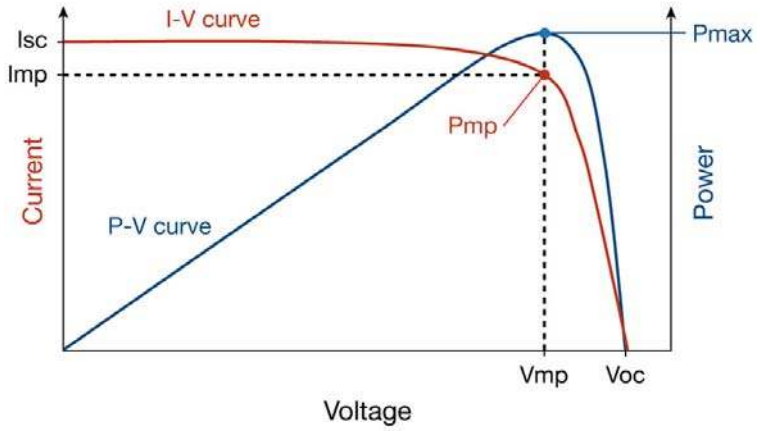

Figure 2.10. Power curve of a PV module [27].

The PV modules in a photovoltaic system can operate at different points within the IV curve. However, the maximum power output can only be achieved if the PV module operates at maximum voltage V_{mp} and current I_{mp} point. This corresponds to the maximum power point P_{mp} as shown in Figure 2.10. Hence, the PV systems have built in MPPT (Maximum Power Point Tracking) control with appropriate power electronics interface which ensures maximum utilization of the available power.

2.1.3. Transient stability of PV-hydro microgrid systems

Transient stability of a power system is defined as its ability to maintain synchronism when there are instances of severe transient disturbances. A power system is said to be stable if it can maintain its state of equilibrium under normal conditions as well as after being subjected to a disturbance without losing synchronism. When a power

system loses synchronism, the rotors of the synchronous machines in the power system run at a speed, higher or lower than that which is required for the generation of the voltage at the rated frequency. This causes large fluctuations in the output of the machines making it unstable. It can no longer return to the rated speed which leads to triggering of protection systems.

The rate of change of frequency, $\frac{\mathrm{d}(\Delta \mathrm{f})}{\mathrm{dt}}$, of a power system can be defined by a linearized model of power system frequency dynamics as [28]

$$\frac{d\Delta f}{dt} = \frac{f_0}{(2HS_b)}(\Delta P_m - \Delta P_{Load}) \tag{2.2}$$

where, $\frac{\mathrm{d}\Delta \mathrm{f}}{\mathrm{dt}}$ is the rate of change of frequency, f_0 is the rated system frequency, H is the inertia constant of the power system, S_b is the apparent power rating of the power system, P_m is the mechanical power input and P_{Load} is the electrical load. It is clear from Equation (2.2) that the rate of change of frequency and consequently the frequency deviation depends directly to the imbalance between the mechanical power input and the electrical power output. But, the rate of change of frequency is inversely proportional to the inertia constant of the power system. The inertia constant, 'H' is used to represent the inertia of a power system normalized to its capacity and defined as [24]

$$H = \frac{Stored\ energy\ at\ rated\ speed\ of\ rotor}{Apparent\ power\ rating} = \frac{1}{2}\frac{J\omega^2}{S_b} \tag{2.3}$$

where, J is the moment of inertia, ω is the speed of the rotor of the machine(s). Lower is the inertia constant of the system higher is the rate of change of frequency and frequency deviation in the system. The inertia constant is low in PV-hydro isolated microgrid

systems and in isolated microgrid in general. This makes isolated power systems susceptible to higher frequency deviations and poor transient stability.

In hydro only microgrids, the inertia of the large masses from the synchronous generators can handle the frequency deviations due to load and generation changes. When PV systems without any rotating mass are added, the system size increases but the inertia does not. The hydro system controls the frequency of the PV-hydro system and typically cannot handle the fast dynamics that are introduced by the addition of PV. The frequency deviations in the system due to load/generation variations and/or PV fluctuations may go out of limits. Hence, the transient stability of such systems becomes poor. This also limits the integration of PV into the hydro system.

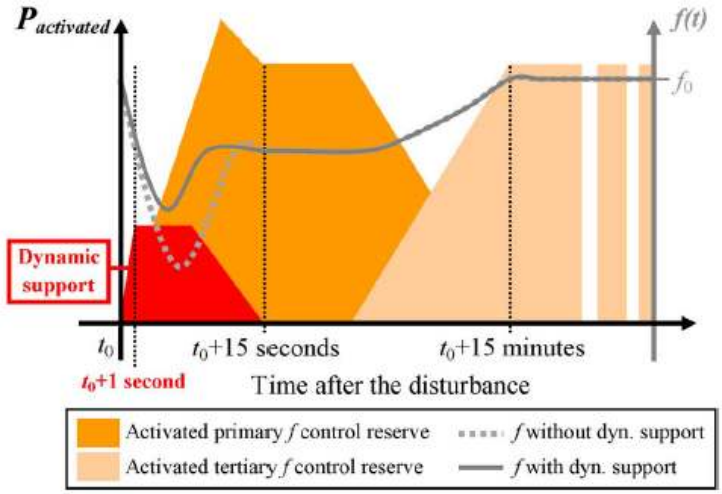

Figure 2.11. Activation of frequency reserves vs time after disturbance [3].

Whenever there is a frequency variation in a power system, the inertial reserve of the power system acts to counter act the initial frequency deviation before the primary reserve brings the system back to a steady value [3]. Conventionally, the large rotational masses of synchronous generators are responsible for providing a significant amount of

inertia to large power systems. Synchronous generators release or absorb kinetic energy whenever there is a change in grid frequency. The rate at which the kinetic energy is released depends upon the ROCOF. But with a high penetration of PV, the overall inertia of the system decreases in proportion to the increase in system size. Hence, added inertial response is needed to provide better dynamic frequency support during transient periods of frequency deviations. Figure 2.11 shows that the addition of dynamic frequency support in a power system reduces the frequency deviations in the system. Moreover, the dynamic frequency reserve has to be fast acting for it to be useful.

2.2. Modeling and control of three phase voltage source inverters

Modeling of three phase voltage sources inverters involves the representation of physical inverter systems using mathematical equations or more specifically transfer functions. These mathematical models can be utilized for the design of controllers for three phase voltage source inverters. Often, DQ (Direct and Quadrature axis) transformation theories are used to design the controllers for the inverter systems.

2.2.1. Three phase voltage source inverters

Three voltage source inverters convert DC voltages to an AC voltage of desired voltage amplitude and frequency. The voltage amplitude and frequency is controlled by pulse width modulation techniques and hence these inverters are known as pulse width modulated inverters [29]. Pulse modulation techniques are used to achieve an AC waveform output from the inverter close to a sinusoidal shape. Often low pass filters are added at the output of the pulse width modulated inverters to help achieve sinusoidal waveforms with low harmonics content. Inverters find applications in grid integration of renewable sources, power quality improvement, standby / uninterruptable power supplies,

electric vehicles and electric drives in industries among others. Inverters are designed using electronic switches like BJTs, IGBTs, and MOSFETs etc. These switches are controlled by pulse width modulated signals which are generated by one of the many available modulation techniques. The inverters are referred to as DC-AC converters and are bidirectional i.e. the same converters can be operated as a rectifiers (convert AC signals to DC) or inverters (convert DC signals to AC) based on the switching signals provided to the switches of the converter.

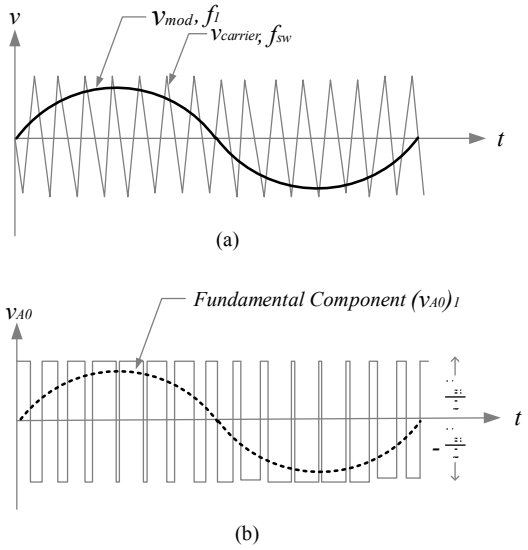

Figure 2.12. (a) Single phase sine wave modulation (b) Output voltage of the single phase inverter and its fundamental component.

Sinusoidal pulse width modulation (SPWM) is one of the many modulation techniques to used generate the switching signals for the inverter. A sinusoidal modulating signal V_{mod} with a frequency f_1 is compared with a triangular carrier wave $V_{carrier}$ with a frequency f_{sw} as shown in Figure 2.12 (a). The frequency of the triangular carrier wave determines the switching frequency of the switching signals and frequency of the

sinusoidal modulating signals determines the frequency of the fundamental component of the inverter output voltage. The modulating signal modulates the switch duty ratio. The ratio of the magnitude of the modulating voltage to the carrier voltage is defined as the amplitude modulation ratio, m_a, as [30]

$$m_a = \frac{|V_{mod}|}{|V_{carrier}|} \tag{2.4}$$

where, $|V_{mod}|$ and $|V_{carrier}|$ represents the magnitude of the modulating and the carrier signal respectively. The magnitude of the carrier wave is generally kept constant, hence it is the magnitude of the modulating signal that controls the amplitude modulation ratio. Similarly, the ratio of frequencies of the carrier signal and the modulating signal is defined as the frequency modulation ratio, m_f, as [30]

$$m_f = \frac{f_{sw}}{f_1} \tag{2.5}$$

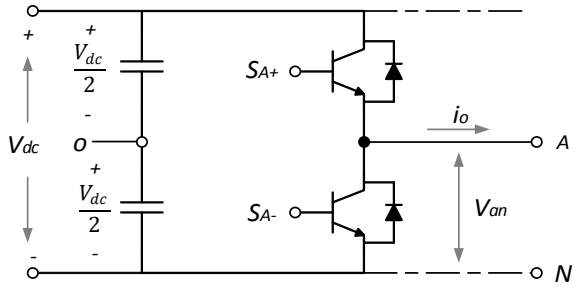

Figure 2.13. Single phase pulse width modulated inverter.

In the single phase inverter shown in Figure 2.13, the switches S_{A+} and S_{A-} are controlled by the switching signals generated from the comparison between modulating signal and the carrier signal. The generated output voltage v_{A0} is generated based on the following logic,

$$If\ v_{mod} > v_{carrier}\ ; \quad S_{A+}\ is\ ON; \quad v_{A0} = \frac{1}{2}V_{dc}$$

$$If\ v_{mod} < v_{carrier}\ ; \quad S_{A-}\ is\ ON; \quad v_{A0} = -\frac{1}{2}V_{dc}$$

Figure 2.12 (b) shows the output voltage v_{A0} of the single phase inverter shown and its fundamental component for $m_a = 0.8$ and $m_f = 15$. The amplitude of the fundamental component of the output voltage, $|v_{A0}|_1$, of the inverter is given by [30]

$$(|v_{A0}|)_1 = m_a\,(\frac{V_{dc}}{2}) \tag{2.6}$$

where, V_{dc} is the DC side voltage and m_a is the amplitude modulation ratio.

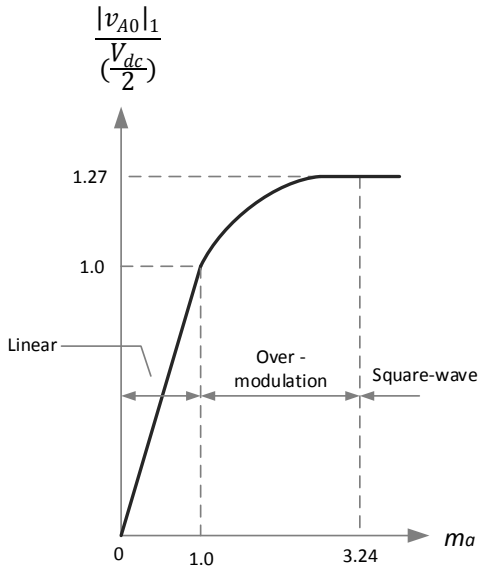

Figure 2.14. Inverter output voltage normalized to input DC voltage vs. amplitude modulation ratio.

It can be seen that there exists a linear relationship between the input DC voltage and the output AC voltage which is given by the amplitude modulation ratio as shown in Figure 2.14. When the amplitude modulation is higher than 1.0, over-modulation occurs

and the amplitude of the fundamental frequency component does not vary linearly with the amplitude modulation ratio. Moreover, at very large modulation indexes the inverter output voltage results in square wave output instead of multiple pulses [30].

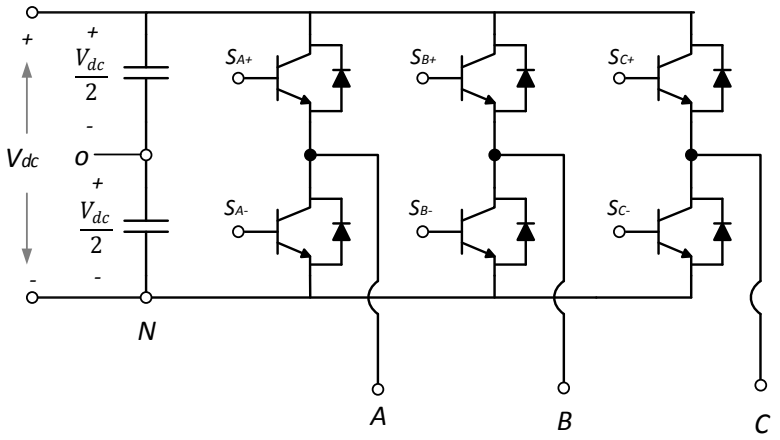

Figure 2.15. Three phase pulse width modulated inverter.

Three phase pulse width modulated inverters consists of three leg switches one for each phase as shown in Figure 2.15. The switching signals are generated in such a manner that the output voltage produced by each phase is displaced from one another by 120°.

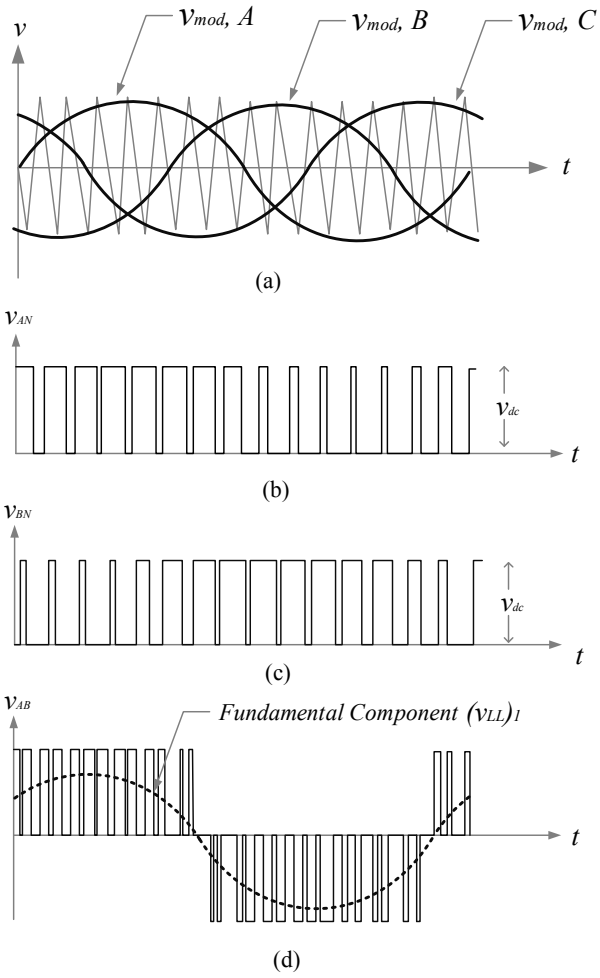

Figure 2.16. Three phase inverter waveforms.

Sinusoidal pulse width modulation techniques can also be used to generate the switching signals for the six electronic switches in the three phase inverter. But, instead of just the single modulating signal, three modulating signals which are 120° out of phase from each other are compared with the triangular carrier wave as shown in Figure 2.16(a). The output voltage of each leg of the inverter depends on the DC voltage V_{dc} and the amplitude modulation ratio. The output voltage waveform of the two phase A and B with respect to the neutral point N is shown in Figure 2.16(b) and (c) respectively. Similarly, the output line to line voltage v_{AB} along with its fundamental component is shown in

Figure 2.16(d). The peak value of the fundamental component of the output voltage for phase A with respect to the neutral, $|V_{AN}|_1$, is given by [30]

$$|V_{AN}|_1 = m_a \frac{V_{dc}}{2} \tag{2.7}$$

Hence, the output voltage of the three phase inverter is thus controlled by amplitude modulation ratio.

2.2.2. Three phase transformation theory

Three phase transformation is a mathematical technique used to simplify analysis/ study of power systems by decoupling time varying quantities in a power system. This technique considerably reduces the complexity of solving power system problems involving time variant variables. Moreover, these mathematical transformations also help in design of models and control systems for power systems. Two mathematical transformations are generally used,

(1) Stationary frame / Clarke's transformation

(2) Rotating frame / Park's transformation

Clarke's transformation converts three phase time varying quantities (a-b-c) into two phase orthogonal time varying quantities (α-β). Figure 2.17 shows the a-b-c and α-β coordinates, the α-β coordinates does not rotate like the a-b-c coordinates thus the name stationery transformation. The α axis is aligned with the a axis and β axis is orthogonal to the α axis.

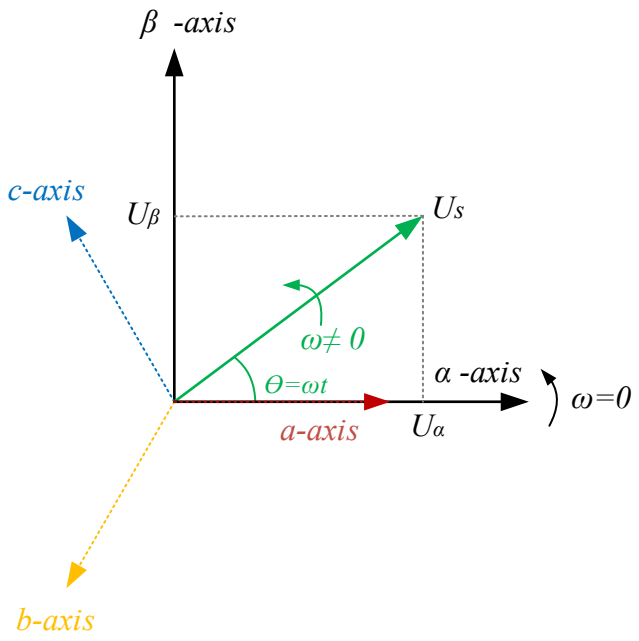

Figure 2.17. Representation of stationery / Clarke's transformation.

A rotating vector U_s which is a three phase quantity consisting of a, b and c axis components can be represented in the α-β frame by two components using U_α and U_β using the Clarke's transformation. The vector U_s can be represented as

$$\overrightarrow{U_s} = |\overrightarrow{U_s}| \angle \theta = U_\alpha + jU_\beta = \frac{2}{3}\left(u_a + u_b e^{j\frac{2\pi}{3}} + u_c e^{-j\frac{2\pi}{3}}\right) \tag{2.8}$$

where,

$$|\overrightarrow{U_s}| = \sqrt{{U_\alpha}^2 + {U_\beta}^2} \tag{2.9}$$

$$\theta = \tan^{-1}\left(\frac{U_\beta}{U_\alpha}\right) \tag{2.10}$$

Also,
$$e^{\pm j\frac{2\pi}{3}} = \cos\left(\frac{2\pi}{3}\right) \pm j \sin\left(\frac{2\pi}{3}\right) \tag{2.11}$$

Also, the zero sequence component, u_0, is given by

$$u_0 = \frac{1}{3}\,(u_a + u_b + u_c) \tag{2.12}$$

From Equations (2.8), (2.11) and (2.12) the following relation can be obtained,

$$\begin{bmatrix} u_\alpha \\ u_\beta \\ u_0 \end{bmatrix} = \frac{2}{3}\begin{bmatrix} 1 & \cos(\frac{2\pi}{3}) & \cos(-\frac{2\pi}{3}) \\ 0 & \sin(\frac{2\pi}{3}) & \sin(-\frac{2\pi}{3}) \\ \frac{1}{2} & \frac{1}{2} & \frac{1}{2} \end{bmatrix}\begin{bmatrix} u_a \\ u_b \\ u_c \end{bmatrix} \tag{2.13}$$

$$\text{or, } [F_{\alpha\beta 0}] = [C][F_{abc}] \tag{2.14}$$

where, [C] is known as the Clarke transformation matrix. The inverse transformation from α-β coordinates to a-b-c is given by the inverse Clarke transformation matrix as

$$[F_{abc}] = [C]^{-1}[F_{\alpha\beta 0}] \tag{2.15}$$

Based on α and β voltage and current quantities the active power, p, and the reactive power, q, consumed by a certain load or supplied by a source can be calculated using the following equations [31]

$$Active\ power\ (p) = u_\alpha i_\alpha + u_\beta i_\beta = \bar{p} + \tilde{p} \tag{2.16}$$

$$Reactive\ power\ (q) = u_\alpha i_\beta - u_\beta i_\alpha = \bar{q} + \tilde{q} \tag{2.17}$$

where, i_α and i_β are the alpha and beta components of the current and the tilda values $\tilde{p}$ and $\tilde{q}$ represent the active and the reactive power due to harmonics and imbalance respectively.

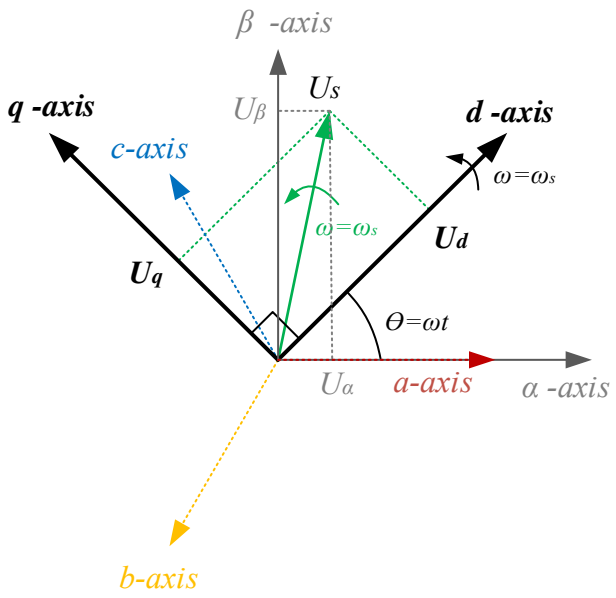

Figure 2.18. Representation of rotating / Park's transformation.

The Park's transformation converts three phase time varying quantities (a-b-c) into two phase orthogonal time invariant quantities (d-q / direct-quadrature). Figure 2.18 shows the a-b-c and d-q coordinates, the d-q coordinates rotates along with a-b-c co-ordinates in the synchronous speed ω_s thus the name rotating transformation. The d and q axes are orthogonal to each other. A rotating vector U_s which is three phase quantity consisting of a, b and c axis components can be represented in the d-q frame by two components using U_d and U_q using the Park's transformation. The Park transformation is an extension of the Clarke transformation. To perform the Park transformation on three phase quantities a-b-c, first a a-b-c to α-β-0 transformation is performed using the Clarke transformation in stationery reference frame. Then, followed by an α-β-0 to d-q-0 transformation in a rotating reference frame, which is rotation of the space vector $\overrightarrow{U_s} = U_\alpha + jU_\beta$[32]. The vector U_s can be represented as

$$\overrightarrow{U_s} = U_d + jU_q = (U_\alpha + jU_\beta).e^{-j\omega t} = \frac{2}{3}\left(u_a + u_b e^{j\frac{2\pi}{3}} + u_c e^{-j\frac{2\pi}{3}}\right).e^{-j\omega t} \quad (2.18)$$

From Equations (2.8), (2.11) and (2.18) the following relation can be obtained as

$$\begin{bmatrix} u_d \\ u_d \\ u_0 \end{bmatrix} = \frac{2}{3}\begin{bmatrix} \cos(\omega t) & \cos(\omega t - \frac{2\pi}{3}) & \cos(\omega t + \frac{2\pi}{3}) \\ -\sin(\omega t) & -\sin(\omega t - \frac{2\pi}{3}) & -\sin(\omega t + \frac{2\pi}{3}) \\ \frac{1}{2} & \frac{1}{2} & \frac{1}{2} \end{bmatrix}\begin{bmatrix} u_a \\ u_b \\ u_c \end{bmatrix} \quad (2.19)$$

$$\text{or, } [F_{dq0}] = [P][F_{abc}] \quad (2.20)$$

Where [P] is known as the Park transformation matrix. The inverse transformation from d-q coordinates to a-b-c is given by the inverse Park transformation matrix as

$$[F_{abc}] = [P]^{-1}[F_{dq0}] \quad (2.21)$$

Based on the d and q voltage and current quantities the active power , p, and the reactive power, q, consumed by a certain load or supplied by a source can be calculated using the following equations [33],

$$Active\ power\ (p) = \frac{3}{2}(u_d i_d + u_q i_q) \quad (2.22)$$

$$Reactive\ power\ (q) = \frac{3}{2}(u_d i_q - u_q i_d) \quad (2.23)$$

Where, i_d and i_q are the d and the q axis components of the currents respectively. If the synchronous rotating frame shown in Figure 2.18 is aligned to rotate with the voltage U_s, the d-axis component will correspond to the magnitude of the voltage (i.e., $u_d = u_{a\_peak}$) while the q-axis component u_q will be zero. Equations (2.22) and (2.23) can thus be modified as

$$Active\ power\ (p) = \frac{3}{2}\, u_d i_d \tag{2.24}$$

$$Reactive\ power\ (p) = \frac{3}{2}\, u_d i_q \tag{2.25}$$

Hence, it is clear that using (2.24) and (2.25) decoupled control of active and reactive power is possible by controlling the d-q current components independently.

2.2.3. DQ modeling of three phase voltage source inverters

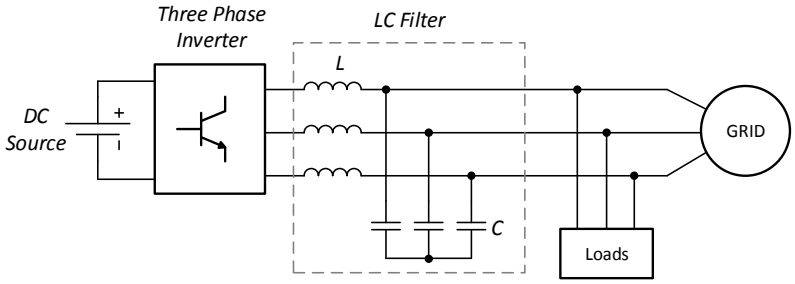

Figure 2.19. Grid connected three phase pulse width modulated inverter with LC filter and loads.

Figure 2.19 shows a grid connected three phase pulse width modulated inverter followed by a LC filter and some local loads. The LC filter is a second order low pass filter which filters the unwanted harmonics created by switching of the electronic switches inside the three phase inverter. To develop a model of the three phase grid connected inverter, the system shown in Figure 2.18 can be represented by ideal three phase controlled voltage sources, neglecting the effect of switching as shown in Figure 2.20. In this simplified representation the grid is represented by a three phase voltage source along with its equivalent impedance values and the local loads are represented by current sources.

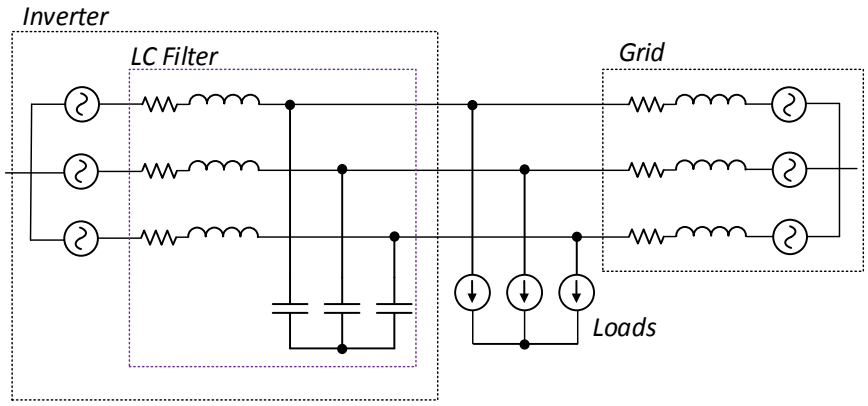

Figure 2.20. Three phase inverter with the grid and inverter replaced by ideal sources.

To further simplify the model, the three phase representation of the inverter system of Figure 2.20 can be represented by a per phase model as shown in Figure 2.21. The effect of the grid and the source can be represented by a single current source which is equal to the net current. This model is however in the a-b-c domain. The variables in this model are time variant and it is difficult to apply principles of linear control design to design the controllers for the inverter system. Hence, a d-q equivalent model is required for design of the appropriate controllers for the system.

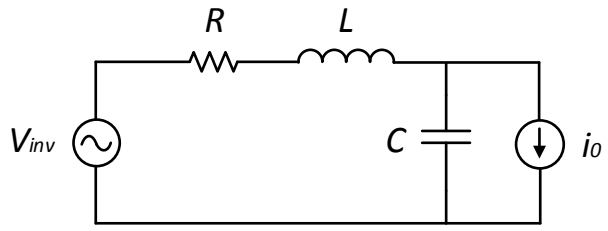

Figure 2.21. Per phase equivalent model of three phase inverter.

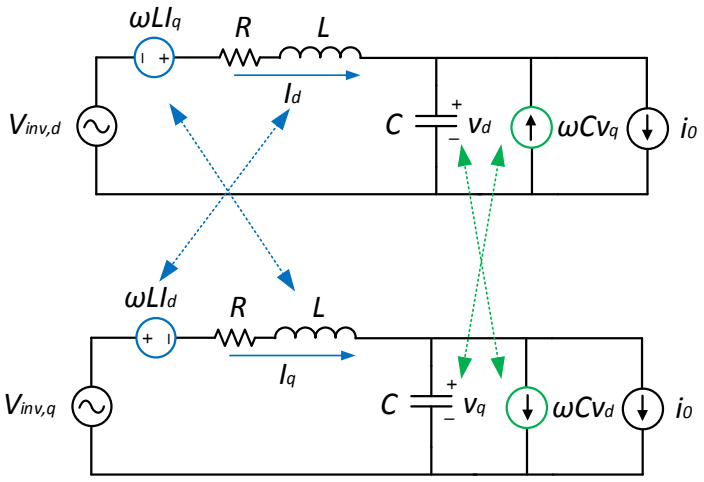

Figure 2.22. DQ equivalent model of three phase inverter.

Figure 2.22 shows the equivalent d-q model of the grid connected three phase inverter. The d-q equivalent model consists of two circuits, one each for the d-axis and q-axis. The model is similar to the single phase model shown in Figure 2.21 except for the additional cross-coupling terms that are introduced. In the d-axis circuit, an additional voltage source ωLI_q is introduced which supports the inverter voltage $V_{inv,d}$ and an additional current source ωCV_q. It is important to note that the in the d-axis circuit the additional terms are introduced by the q-axis current and voltage components rather than that of the d-axis components. Hence, due to this cross-coupling effect these additional terms are referred as cross-coupling components. Similarly, in the q-axis circuit an additional voltage source ωLI_d is introduced which opposes the inverter voltage and an additional current source $V_{inv,q}$ is also introduced along with an additional current source ωCV_d. The variables obtained in this model are now time invariant and allows for easier application if linear control theories to design controllers for the system.

2.2.4. DQ-based control of three phase voltage source inverters

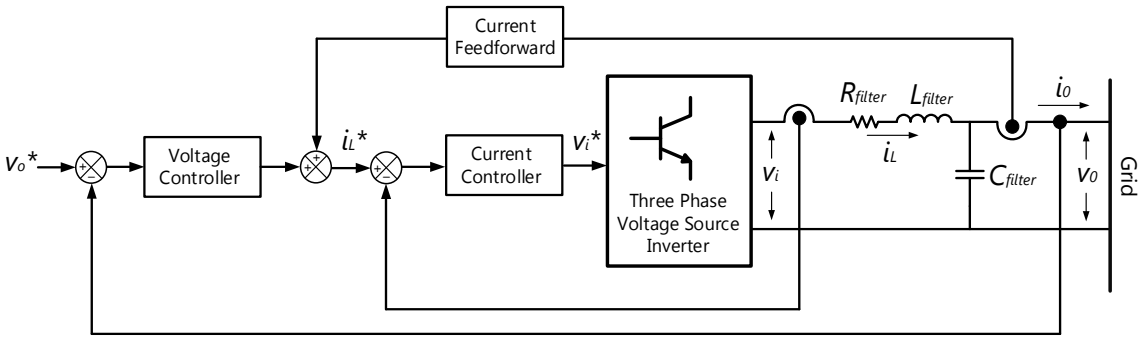

Figure 2.23. Typical control schematic of a three phase inverter.

Figure 2.23 shows a typical control schematic of a three phase pulse width modulated inverter along with its voltage and current control loops. The closed loop control is achieved with a two–loop structure. The innermost control loop is used to control the current. This is the loop around the filter inductor and the voltage source inverter which creates a controlled current source. Similarly, the outer loop is used to control the output voltage of the inverter. The voltage loop is used to track the slow changes in the reference voltage v_0^* and minimize the errors that are produced by variations in the output current i_0. A current feedforward helps to provide added rejection of disturbance from any other sources.

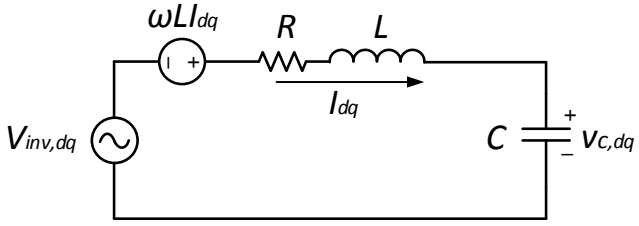

Figure 2.24. Simplified d-q equivalent model for current controller design.

If the variation of the current over the inductor is always proportional to the voltage applied across it the d-q equivalent model shown in Figure 2.22 can be further simplified as shown in Figure 2.24. In this simplified model, the current through the inductor depends on the voltage difference between the voltage applied by the voltage source inverter and the capacitor voltage. The cross coupling terms and the voltage across the capacitor are considered to be disturbance to the control system design. Now, using the KVL equation transfer function of the plant, G(s), can be modeled as

$$G(s) = \frac{I_{dq}}{V_{inv,dq}} = \frac{\frac{1}{L}}{s + \frac{R}{L}} \tag{2.26}$$

where, s is the Laplace transform variable, R is the internal resistance of the filter inductor and R is the internal resistance of the filter inductor. This gives a current controller topology as shown in Figure 2.25:

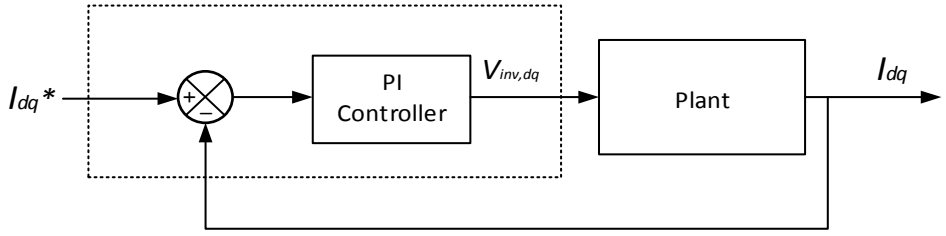

Figure 2.25. Simplified d-q equivalent model for current controller design.

Now, if the neglected cross-coupling terms and the voltage across the capacitor are added, this gives a current controller topology as shown in Figure 2.26,

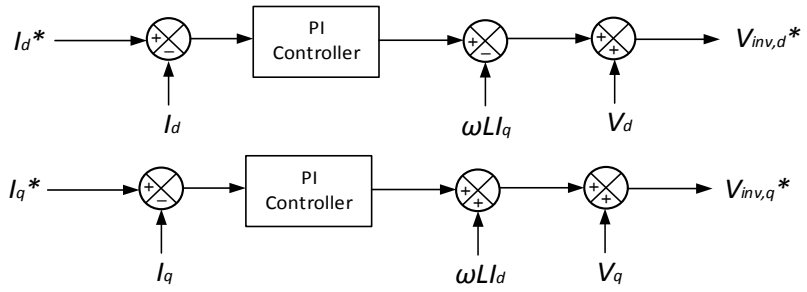

Figure 2.26. Current controller topology considering the cross coupling terms and the capacitor voltage feedforward.

2.3. Virtual synchronous machines

Virtual synchronous machine (VSM) is an energy storage device with power electronics and a dispatching algorithm that makes it behave as a synchronous generator for short energy storage requirements.

2.3.1. Operating principle of virtual synchronous machines

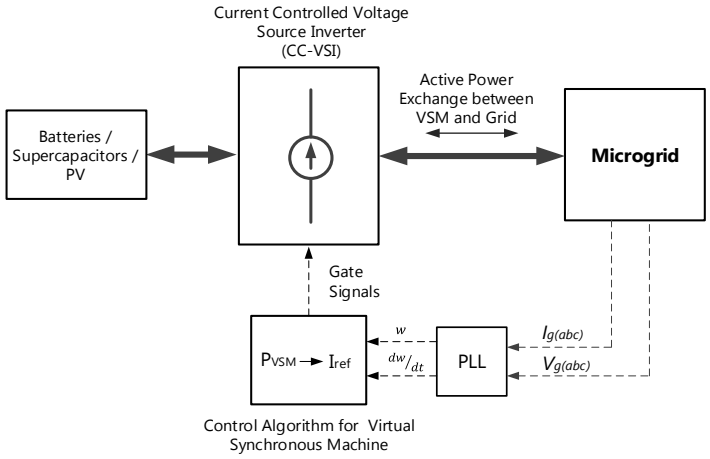

Figure 2.27. Block diagram of a virtual synchronous machine.

The energy storage in a VSM can be any DC source like small batteries, super-capacitors or even PV as shown in Figure 2.27. It emulates the inertial and damping properties of a synchronous generator by injecting active power when there is a negative

change in frequency and absorbing active power when the change in frequency is positive. The output power of the VSM, P_{VSM} emulates the behavior of a synchronous generator based on the following equation [4]

$$P_{VSM} = K_I \frac{d(\Delta f)}{dt} + K_P(\Delta f) \tag{2.27}$$

where, K_I is the emulated inertia constant and K_P is the emulated damping constant. Both are negative constants that counteract the rate of change of frequency $\frac{d(\Delta f)}{dt}$ and the frequency deviation Δf respectively. The first term in Equation (2.27) makes the VSM operate during the transient period to reduce the rate of change of frequency. The second is the droop part that returns the frequency to a nominal value. The inertia constant, K_I, and the damping constant, K_P, can be calculated as [22]

$$K_I = \frac{P_{VSM\_NOM}}{(\frac{d\Delta f}{dt})_{max}} \tag{2.28}$$

$$K_p = \frac{P_{VSM\_NOM}}{(\Delta f)_{max}} \tag{2.29}$$

where, P_{VSM_NOM} is the nominal power rating of the VSM, Δf is the maximum change in frequency and $\frac{d\Delta f}{dt}$ is the maximum change in the rate of change in frequency. K_P emulates the effects of the damper windings of a real synchronous generator. Using just the inertial term K_I in the VSM may reduce the deviation of the rotor speed in the event of a disturbance but reduces the natural frequency and the damping ratio of the system [23]. The maximum inertia that a VSM can emulate, $H_{emulated}$, can be calculated as [4]

$$H_{emulated} = \frac{K_I f_0}{2P_g} \tag{2.30}$$

where, P_g is the total size of system , K_I is the inertia constant and f_0 is the rated system frequency.

The phase locked loop (PLL) shown in Figure 2.27 measures the microgrid frequency and the rate of change of frequency using the microgrid voltage $V_{g(abc)}$. The PLL also provides the phase angle for the d-q based control of the voltage source inverter [4] . The control algorithm then calculates P_{VSM} using Equation (2.27) to generate the reference current I_{ref} for the controller. The controller then based on the feedback current signal $I_{g(abc)}$ generates the necessary gating signals for the voltage source inverter, thus exchanging the calculated active power between the microgrid and the DC energy storage.

2.3.2. Virtual synchronous machine topologies

Among the many topologies used for the design of virtual synchronous machines following are the more prominent topologies:

(a) VSYNC's virtual synchronous generator

(b) IEPE's virtual synchronous generator

(c) ISE lab's virtual synchronous generator

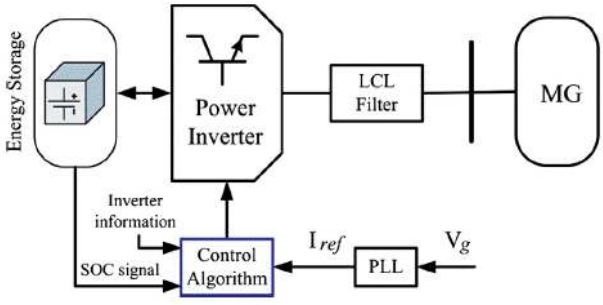

Figure 2.28. Block diagram of a VSYNCs VSM topology [4].

The topology used by VSYNC research group to implement virtual synchronous machine is shown in Figure 2.28 [34]. The energy storage element is connected with the microgrid through a power inverter and an LCL filter to remove the switching noises. The power exchange between the energy storage and the microgrid is achieved by a current control algorithm. Current reference for the current control algorithm is generated by the phase locked loop (PLL) using the microgrid voltage V_g. The PLL helps to emulate the electromechanical characteristics similar to that of a synchronous generator. Moreover, in this topology the PLL also provides the phase angle reference required for d-q based current controller design. Figure 2.29 (a) shows a more detailed illustration of the

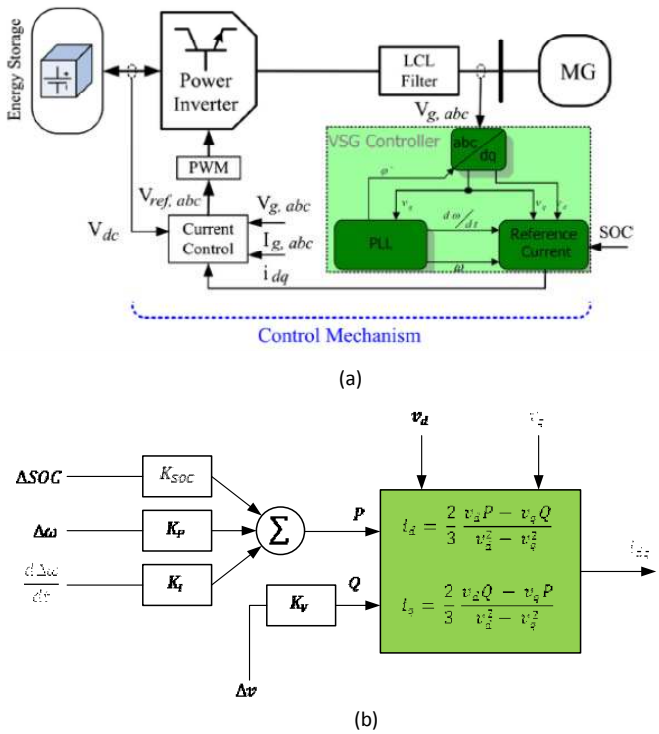

Figure 2.29. (a) Detailed illustration VSYNC's VSM topology (b) Details of reference current generator block.

topology used by VSYNC research group. As discussed earlier, the PLL using the microgrid voltage sets up the reference currents by measuring the rate of change of frequency $\frac{d\omega}{dt}$ and frequency variation ω. An additional signal SOC is also used in the calculation of the reference current. The SOC feedback signal is used to ensure that the state of charge of the energy storage element is always maintained in the desired level for proper VSM operation. The current control then based on the reference current i_{dq} generates the PWM gate signals to drive the power inverter. The details of the reference current block is shown in Figure 2.29 (b). Using the feedback signals $\frac{d\Delta\omega}{dt}$, Δω and ΔSOC the active power reference is setup. If it is desired the VSM can also be made to exchange reactive power with the microgrid. For this, the change in microgrid voltage Δv is used to setup the reference reactive power. The equivalent direct axis current, i_d, and quadrature axis current, i_q, to generate the reference active power and reactive power is then calculated based on the following equations [4]

$$i_d = \frac{2}{3}\frac{v_d P - v_q Q}{v_d^2 + v_q^2} \tag{2.31}$$

$$i_q = \frac{2}{3}\frac{v_d Q + v_q P}{v_d^2 + v_q^2} \tag{2.32}$$

Where, P is the reference active power, Q is the reference reactive power, v_d direct axis voltage and v_q is quadrature axis voltage.

IEPE's topology is another topology used for implementation of virtual synchronous machines. This topology is based in implementing a dynamic model of a generator and then emulating it characteristics using a power inverter and an energy storage element as shown in Figure 2.30 (a) [35]. The model provides either the reference

current or voltage for the “Driver and pulse generator” block using the grid voltage or current respectively. The output power of the virtual synchronous machine and

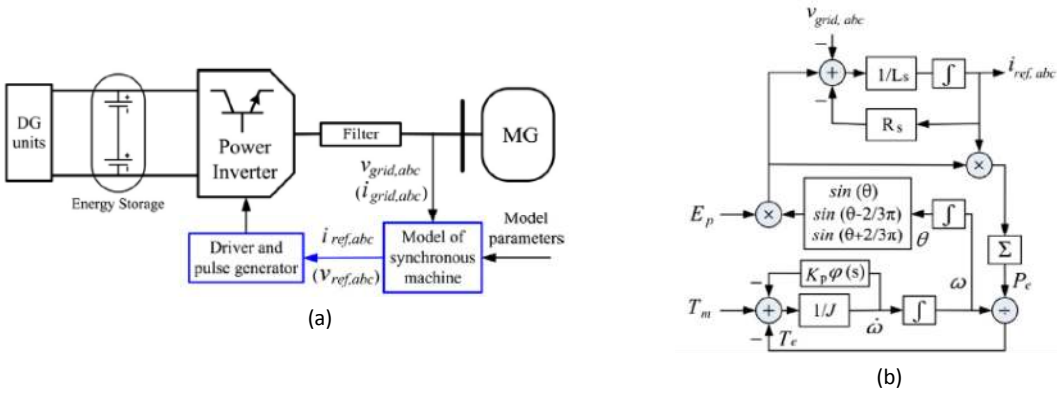

Figure 2.30. (a) Block diagram of IEPE's VSM topology. (b) Simplified dynamic model of synchronous generator.

parameters of the dynamic model of the synchronous generator. Figure 2.30 (b) shows the dynamic model that is implemented at the core of the VSM algorithm. The model produces the reference current $i_{ref,\,abc}$ from the grid voltage $v_{g,\,abc}$. J represents the moment of inertia, R_s is the stator resistance, Ls is the stator inductance, K_p is the mechanical damping factor, Φ(s) is the phase angle compensation term, ω is the angular velocity, θ is the angle of rotation and T_e and T_m are the electrical and mechanical torque.

The topology proposed by ISE lab implements the swing equation based on the difference between the input and output power of the VSM at the core of the control logic [20]. The details of the topology is shown in Figure 2.31. The VSG control block is the main element that makes the power inverter behave as real synchronous machine. It implements the swing equation by calculating the difference between the input power, Pin, and output power, Pout, as [4]

$$P_{in} - P_{out} = J\Delta\omega\frac{d\Delta\omega}{dt} - D\Delta\omega \tag{2.33}$$

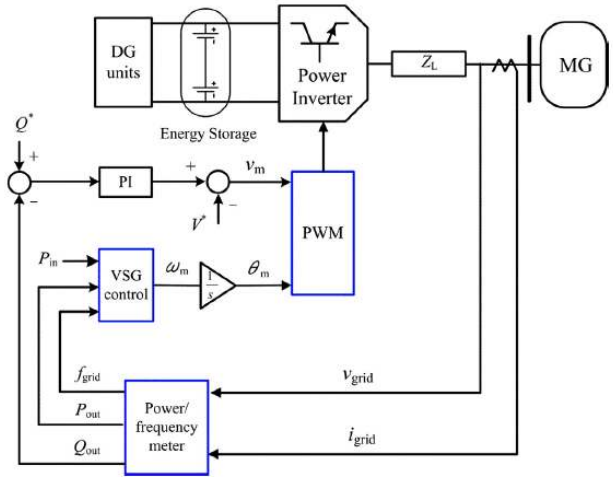

Figure 2.31. Block diagram of ISE lab's VSM topology.

The input to the control block is P_{in}, which is similar to the power available for a real synchronous generator from the prime mover. P_{out} is the output power that will be generated by the power inverter, ω is the angular velocity of the emulated rotor, J is the moment of inertia and D is the damping factor. The swing equation described in Equation (2.33) is solved in each control cycle to generate the momentary frequency ω, which is then integrated to obtain the phase angle θ_m for the PWM generator module. Similarly, Q^* is the reference reactive power that is compared with reactive power generated by the inverter Q_{out} and PI controller is used to generate the reference voltage v_m for the PWM generator. Based on these inputs, the PWM module generates the gate signals which makes the power inverter emulate the characteristics of a real synchronous generator.

2.3.3. Energy storage for microgrid stabilization

Energy storage systems are used in microgrid stabilization by operating them as spinning reserves to provide power balance between power generation and consumption [14]. Energy storage systems in microgrids typically have two major roles,

(a) Short term power balancing, to maintain the short term power balance between generation and consumption and consequently maintain the voltage and frequency stability of the microgrid. This can be categorized as power application of the energy storage systems where the energy storage systems is charged or discharged within small intervals (seconds to minutes).

(b) Long term energy management, to match the generation profile of non – dispatchable energy sources like PV or wind with the profile of the loads within the microgrid. This can be categorized as energy application of the energy storage systems where the energy storage systems is charged or discharged relatively slowly (tens of minutes to hours).

The power application and energy application requires energy storage elements with different characteristics. For power applications, the energy storage system needs to have a fast response coupled with a good cycling life but typically requires minimal energy storage capability. While, the energy application requires high energy capacity with good overall efficiency. The suitability of an energy storage device for particular application is mainly defined by the energy density, power density and the efficiency among other characteristics [36]. The power density is the rated power output divided by the volume of the storage device. Power density can be calculated as,

$$Power\ density = \frac{Rated\ output\ power\ (W)}{Volume\ (l)\ or\ mass\ (kg)} \tag{2.34}$$

Similarly, the energy density is the amount of energy stored in per unit volume or mass. Energy density, E, can be calculated as

$$Energy\ density\ (E) = \frac{Energy\ stored\ (Wh)}{Volume\ (l)\ or\ mass\ (kg)} \tag{2.35}$$

The efficiency of a storage device is the amount of energy that comes out of the device relative to the amount of energy that is put into the device. The efficiency, η, of an energy storage device can be defined as

$$Efficiency\ (\eta) = \frac{Energy\ extracted\ (Wh)}{Energy\ delivered\ to\ the\ device\ (Wh)}\ x\ 100\% \tag{2.36}$$

Different types of energy storage options are used in microgrids based on the function of the energy storage device. Batteries are the most common energy storage used in microgrids. Batteries could be used for short term power balancing or long term application based on the technology used. Various technologies are available like lead-acid, nickel-cadmium, lithium-ion among others. Lead acid batteries are preferred mainly due to its cost and maturity of the technology. Super-capacitors is another storage technology that is being adopted as the costs start to fall. Super-capacitors, have higher power density and a low energy density and mostly suitable for short term power balancing applications. Apart from the power and energy density there are many other factors which are critical for selection of energy storage like the efficiency, cycle life, costs etc. Various types of batteries along with its characteristics are summarized in Table 2.1.

Table 2.1. Characteristics of various energy storage technologies [14, 36].

Technology	**Energy Density (Wh/Kg)**	**Power Density (W/Kg)**	**Cycle Life (No. of Cycles)**	**Efficiency**	**Cost ($/kWh)**
Pb-acid	30-50	500	500-2000	70-90	300-600
Ni-Cd	50-75	990	20000	60-87	1000
Li- Ion	60-200	700	1000-10000	85-100	>600
Super-capacitors	4.5	3500	1000000	85-98	2000

The advantages and disadvantages if various technologies are summarized in Table 2.2.

Table 2.2. Advantages and disadvantages of various storage technologies [14].

Technology	**Advantages**	**Disadvantages**
Pb-acid	• Cost effective • Mature technology	• Low energy density • Cycle life
Ni-Cd	• Energy density • Low maintenance • Lifetime	• Cost • Memory effect
Li- Ion	• Energy density • High efficiency	• Cost
Super-capacitors	• Power density • Long lifetime	• Cost • Energy density

CHAPTER 3 PROCEDURES

Chapter 3 presents the procedures followed to achieve the objectives of this study. The development of the PV-hydro benchmark microgrid is presented first followed by the procedure to perform the transient analysis of the developed system. Next, the steps for design and testing a of three phase grid connected current controlled inverter in PSIM simulation software is presented. The chapter concludes with the implementation of the VSM in OPAL-RT real time digital simulator and also presents the steps to perform the transient analysis of the system with the VSM.

3.1. Development of PV-hydro benchmark microgrid system

The modeling of the 39 kW hydro model and the 25 kWp PV system model will be presented in this section. Moreover, the procedures to perform the transient analysis of the integrated PV-hydro system will be discussed. The transient stability study will include the analysis of the system behavior when there are large short term disturbances in the PV-hydro integrated system like large irradiance changes or a large load or generation change.

3.1.1. Development of 39 kW hydro system model

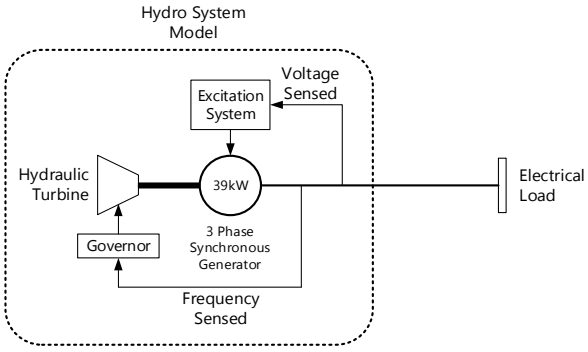

Figure 3.1. Block diagram of the hydro model implemented in MATLAB\Simulink.

The model of the 39 kW hydro system was developed in MATLAB\Simulink software as shown in Figure 3.1. A model of the three phase synchronous machine available in the 'SimPowerSystems' library of MATLAB\Simulink was used to model the generator of hydro system. The main parameters used for the model are summarized in Table 3.1.

Table 3.1. Parameters for synchronous generator model.

Parameter (s)	**Value(s)**
Rotor type	Salient pole
Nominal Power (S_{rated})	39 kVA
Line–to–line rated voltage(V_{L-L})	208 Vrms
Rated frequency(f)	60 Hz
Number of poles(P)	4
Inertia constant (H)	2 s
Normalized reactance in per unit ($X_d, X'_d, X''_d, X_q, X''_q, X_l$)	1.305, 0.296, 0.252, 0.474, 0.243,0.18
Normalized stator resistance in per unit (R_s)	2.85e-3
Time constants (T'_d, T''_d, T''_{q0})	1.01 s, 0.053 s, 0.1 s

The power rating of the synchronous generator was 39 kVA with an output line–to–line voltage of 208 V_{rms} at a rated frequency of 60 Hz which matches the generators capacity at the microgrid lab in SDSU. The rotor of the synchronous machine was salient pole type

with four poles. The inertia constant was assumed to be 2 seconds which is a typical value for synchronous machines of a hydro system [24]. Similarly, the turbine and the governor was modeled using the 'Hydraulic turbine and governor' block available in 'SimPowerSystems' library. The details of this block is shown in Figure 3.2. The main parameters used in the model are summarized in Table 3.2.

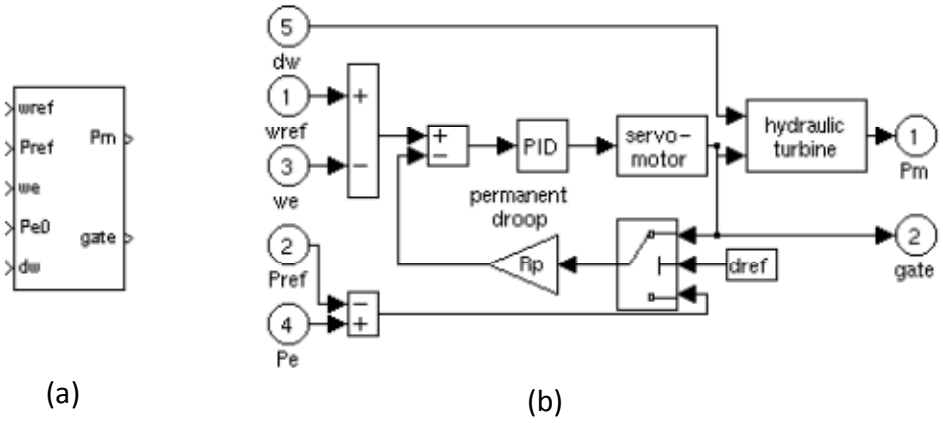

Figure 3.2. (a) Hydraulic turbine and governor block in MATLAB\Simulink. (b) Details of hydrauline turbine and governor block [32].

Table 3.2. Parameters for hydraulic turbine and governor block.

Parameter (s)	**Values (s)**
Servomotor gain (K_a)	5
Servomotor time constant (T_a)	0.07 s
Permanent droop (R_p)	0
Proportional term (K_p)	3.50
Integral term (K_i)	0.54
Derivative term (K_d)	1.06

The excitation system was modeled using the 'Excitation system' block in 'SimPowerSystems' library. The 'Excitation system' block is based on the IEEE standard, IEEE 421.5–1992 for excitation systems of synchronous generators. The electrical loads of the hydro system were modeled using the resistive loads available in the 'SimPowerSystems' library. The complete model of the developed hydro system in MATLAB\Simulink is shown in Figure 3.3.

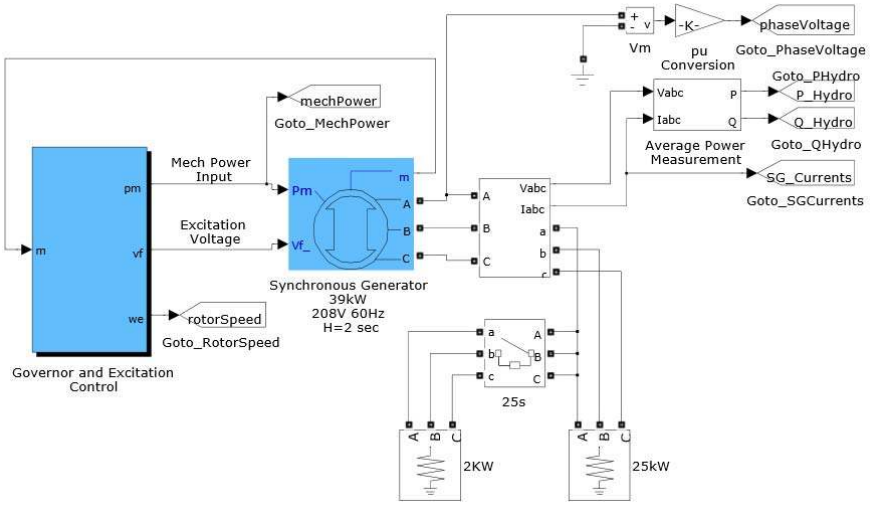

Figure 3.3. MATLAB\Simulink implementation of 39 kW hydro system.

3.1.2. Development of 25 kWp PV system model

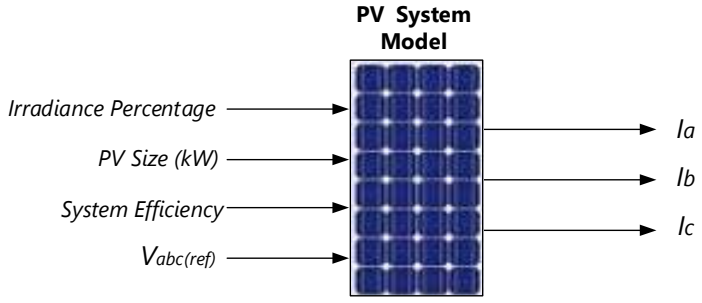

Figure 3.4. PV system model with model inputs and outputs.

The three phase, 25 kWp PV system was modeled using three controlled current sources, one for each phase with no inertial response. A power electronics based converter was not used as a model to reduce the simulation overhead. The overall configuration of the PV system model along with its inputs and outputs is shown in Figure 3.4. The inputs to the model are the irradiance values (normalized to 1000 W/m^2), the peak PV size in kWp, efficiency of the PV system, and the instantaneous values of the reference three phase voltage. The reference voltage was the voltage of the system to which the PV system was to be connected (in this case the output voltage of the hydro system). This voltage was used to provide the phase information for the PV system model so that the output voltage (and current) were in the same phase as the reference voltage. This was accomplished by using the phase locked loop (PLL) as shown in Figure 3.5. Using the input data, the magnitude of the current to be injected was calculated. The magnitude of the current was then multiplied with the sine of the phase of the reference voltage from the PLL to obtain the currents to be injected per phase. The calculated current was then injected into the system using controlled current sources. The MATLAB\Simulink implementation of the model is shown in Figure 3.6 (a) and the details of one of the phases (phase a) in the 'PV Current Injection' block is shown in Figure 3.6 (b). The same model is replicated for phases b and c.

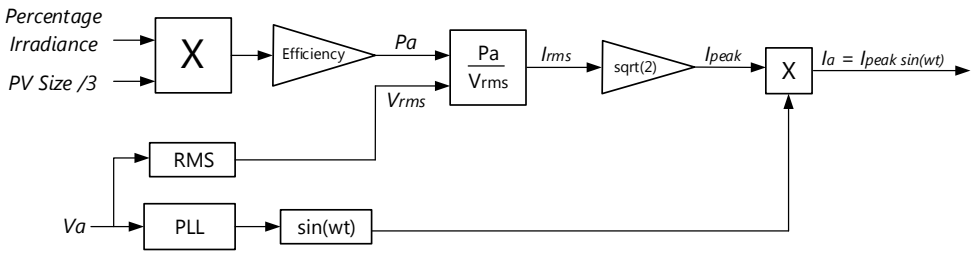

Figure 3.5. Details of a single phase of PV system model.

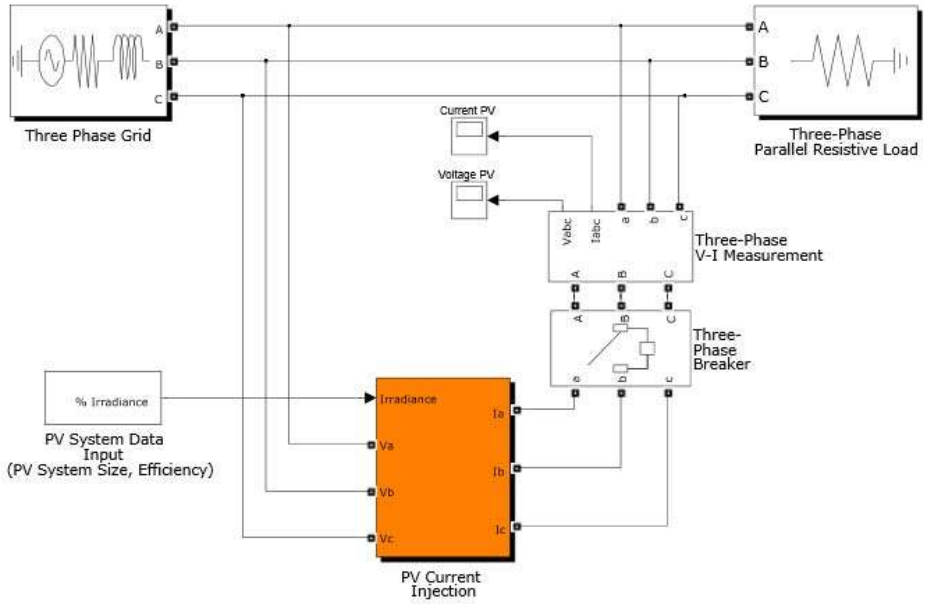

(a)

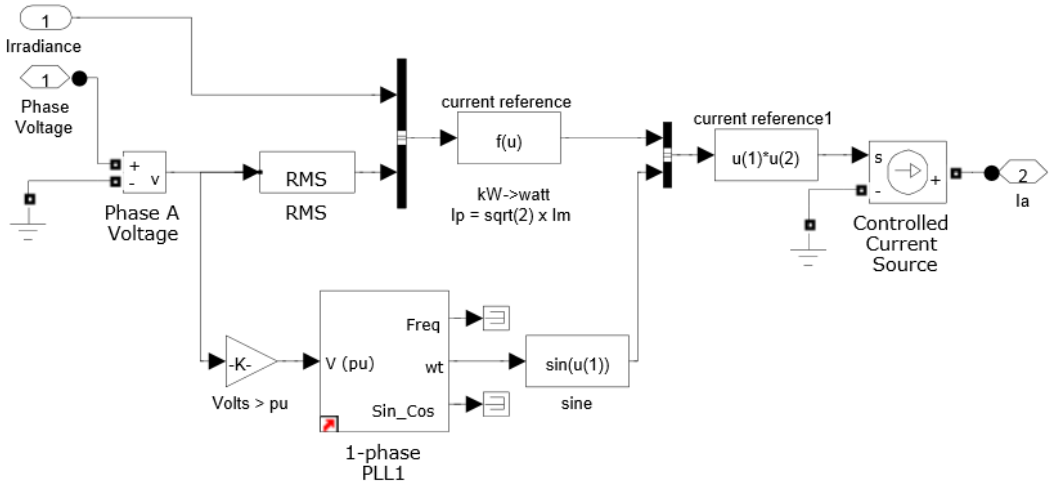

(b)

Figure 3.6. (a) MATLAB\Simulink implementation of PV system model. (b) Details of phase a of PV current injection block.

3.1.3. Implementation of integrated PV-hydro microgrid benchmark model

The 39 kW hydro system model and the 25 kWp PV system was connected together to form the PV – hydro microgrid benchmark model as shown in Figure 3.7. The micorgrid benchmark operates at 208 V_{rms} (line-to-line) with a rated system frequency of 60 Hz. The electrical load connected to the system was purely resistive. The power produced by the hydro model and the PV system model are represented by P_{hydro} and P_{pv} respectively. The hydro system was the master unit which controlled the frequency of the microgrid. The PV system injected power into the system as a current source based on the available irradiance.

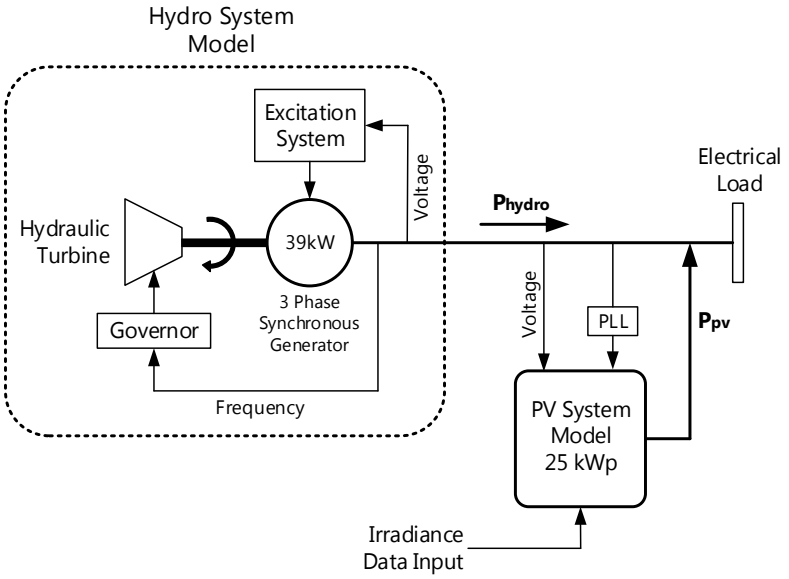

Figure 3.7. Block diagram of PV-hydro benchmark microgrid system.

The transient analysis of the developed microgrid benchmark model was then performed for two cases. The frequency variations in the system was tested first for step changes in irradiance and second for a 250 second snapshot of real irradiance data obtained from the data acquisition in the microgrid lab in SDSU. The objective of this

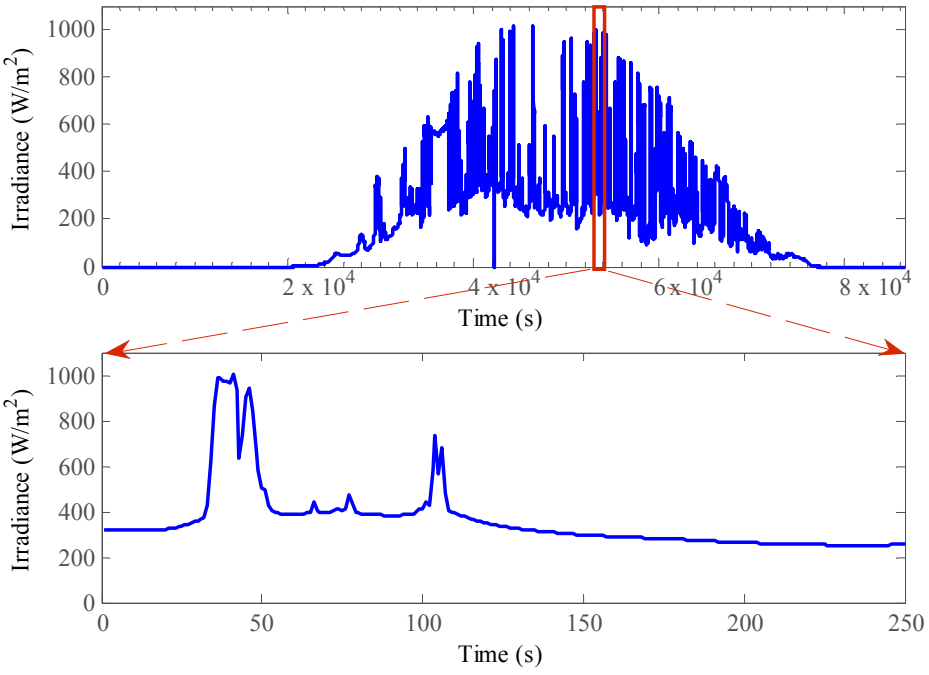

Figure 3.8. 250 second snapshot of real irradiance data obtained from microgrid lab at SDSU from July 19, 2012.

transient analysis was to analyze the stability of the PV-hydro microgrid system to aforementioned cases. The details of the 250 second real irradiance data that was used for the transient analysis is illustrated in Figure 3.8. The data obtained from the data acquisition system was from July 19, 2012 and was sampled once every second. From the irradiance data for the entire day, a 250 second extract was obtained which was the input to the 25 kWp PV system model. This particular snapshot of irradiance data was used for this study because there were large variations in the irradiance data as well as instances of constant irradiance which allowed for transient analysis of the system under different conditions. The simulations were also repeated for PV system sizes of 10 kWp and 15 kWp. The MATLAB\Simulink implementation of the PV-hydro microgrid benchmark system is shown in Figure 3.9.

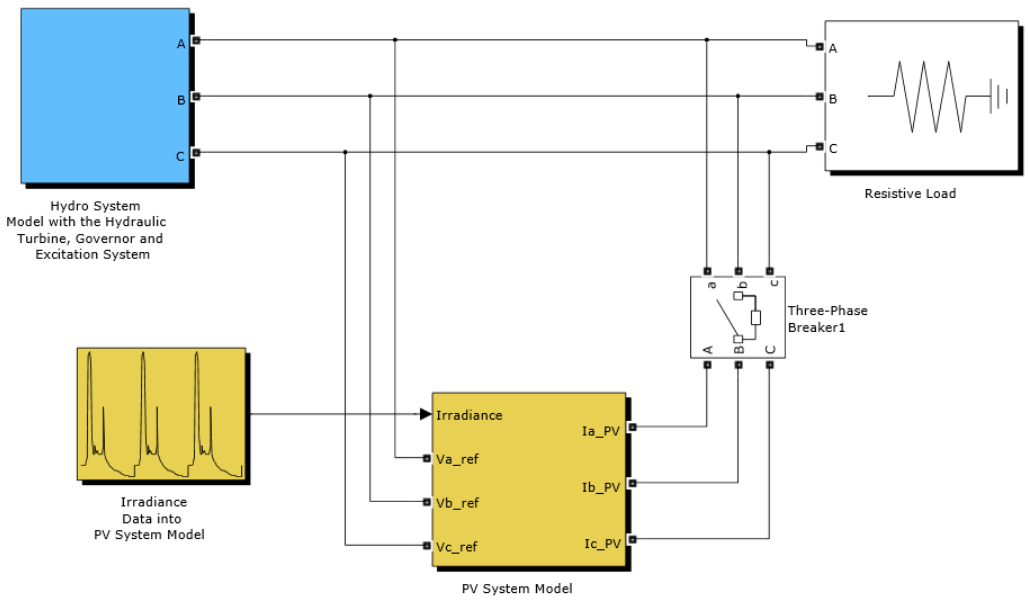

Figure 3.9. MATLAB\Simulink implementation of PV-hydro benchmark microgrid.

3.2. Design of current controlled three phase voltage source inverter

A three phase current controlled inverter was designed to implement the virtual synchronous machine. The current controlled inverter controls the active power exchange between the energy storage element and the PV-hydro microgrid benchmark system based on the VSM algorithm which is described in Section 3.3.

3.2.1. Design of LC filter

The LC filter for the three phase voltage source inverter was represented by a simplified circuit shown in Figure 3.10. V_{inv} represents the unfiltered output voltage of the inverter, L and C are the inductance and capacitance values of the LC filter and R represents the equivalent resistance at the inverter output when the inverter is operating at full power.

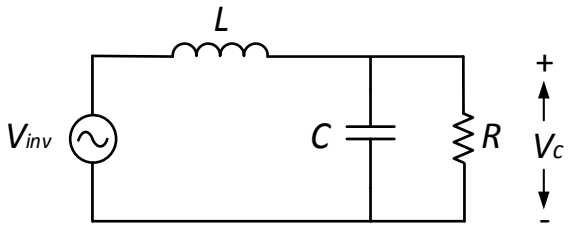

Figure 3.10. LC filter circuit.

The equivalent resistance, R_{eq}, was calculated using

$$R_{eq} = \frac{V^2}{\frac{P}{3}} \tag{3.1}$$

where, V is rated per phase voltage of the inverter and P is the rated power of the inverter. By writing the KVL equations for the circuit of Figure 3.10, the LC filter was modelled by a second order transfer function, $G_{filter}(s)$, using

$$G_{Filter}(s) = \frac{V_c(s)}{V_{inv}(s)} = \frac{\frac{1}{LC}}{s^2 + \frac{1}{CR}s + \frac{1}{LC}} \tag{3.2}$$

where, V_c is the voltage across the output capacitor, V_{inv} is the inverter output voltage before the filter, L is filter inductance, C is the filter capacitance and R is the internal resistance of the filter inductor. Comparing Equation (3.2) with the standard form of a second order transfer function, $G_{second\_order}(s)$, using [37]

$$G_{second\_order}(s) = \frac{\omega_n^2}{s^2 + 2\zeta\omega_n + \omega_n^2} \tag{3.3}$$

where, ζ is damping ratio of the second order system and ω_n is the natural frequency of the second order system. The equations used to calculate the capacitance, C, and inductance, L, for the LC filter were

$$C = \frac{1}{2\zeta\omega_n R} \tag{3.4}$$

$$L = \frac{1}{\omega_n^2 C} \tag{3.5}$$

To the calculate values of the inductance and the capacitance, the natural frequency ω_n was taken to be 1 kHz (= 6283.185 rad/s) which was a decade below the switching frequency of the inverter. Selecting, the natural frequency a decade below the switching frequency ensures adequate attenuation to high frequency noises produced at the inverter output. Similarly, a damping factor ζ of 0.707 was selected as this provides an acceptable trade-off in the response of designed filter system between the system overshoot and response speed [37].

3.2.2. Design of current controller transfer function

The transfer function of the plant, $G_{plant}(s)$, for the design of the current controller was derived using Equation (2.26) as

$$G_{plant}(s) = \frac{I_L(s)}{V_{inv}(s)} = \frac{\frac{1}{L}}{s + \frac{R}{L}} \tag{3.6}$$

The resistance of the inductor was assumed to be 0.1 Ω. The frequency response of the plant was then obtained. The three phase inverter was designed with a switching frequency ω_{sw} of 10 kHz. The cross – over frequency ω_x of the current controller was selected to be 1 kHz (or 6283.18 rad/s) which is a decade below the switching frequency. The 1 kHz cross-over frequency provides fast enough speed response for the designed current controller. Similarly, the phase margin of the loop transfer function (of the plant and the current controller combined) was selected to be 45° at ω_x which provides an

acceptable overshoot for the system. Next, the magnitude, $|G_{plant}(\omega_x)|$, and the phase, $\angle G_{plant}(\omega_x)$, of the plant at the desired cross–over frequency was calculated from the frequency response plot of the plant. It was desirable to achieve a high gain at the low frequencies to ensure that the overall system had minimal steady state error and a higher attenuation at high frequencies to suppress the switching noises in the inverter. Taking these things into consideration a modified PI (Proportional Integral) type 2 controller was selected as the appropriate controller for the current control. The generic transfer function used for the PI type 2 controller, $C_{PI2}(s)$ was [38]

$$C_{PI2}(s) = K_{PI}\frac{1+s\tau}{s\tau}\frac{1}{1+sT_p} \tag{3.7}$$

where, K_{PI} is the proportional gain, τ is the time constant of the controller and T_p is the time constant of the additional pole at high frequency used to attenuate high frequency noises. These constants are labeled in the theoretical frequency response a PI type 2 controller in Figure 3.11.

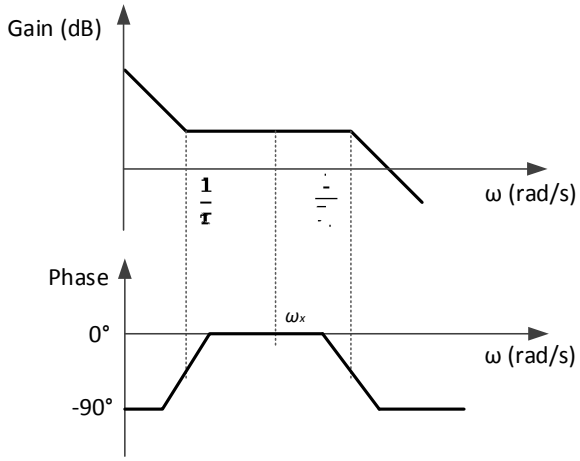

Figure 3.11. Asymptotic frequency response of a PI type 2 controller.

In order to calculate the time constant τ and T_p of Figure 3.11 the boost angle of the controller, θ_{boost} and K factor were calculated such that the controller yielded the desired phase angle at the required cross-over frequency, which in this case was 45° at a cross–over frequency of 1 kHz. The boost angle, θ_{boost}, was calculated using [38]

$$\theta_{boost} = \emptyset + 90° \tag{3.8}$$

where, $$\emptyset = -\left(180° + \angle G_{plant}(\omega_x) - Phase\ Margin\right) \tag{3.9}$$

Using the boost angle, the K factor, was calculated using

$$K = \tan\left(\frac{\theta_{boost}}{2} + 45°\right) \tag{3.10}$$

The time constants τ and T_p which were calculated using

$$\tau = \frac{K}{\omega_x} \tag{3.11}$$

$$T_p = \frac{1}{K\omega_x} \tag{3.12}$$

Finally, the proportional gain, K_{PI}, was calculated as

$$K_{PI} = \frac{1}{\left|G_{plant}(\omega_x)\right|} \tag{3.13}$$

3.2.3. Implementation of current controller in PSIM simulation software

The current control loop designed in Section 3.2.2 was implemented in PSIM simulation software for verification of the design in a grid connected three phase inverter system designed in PSIM. Figure 3.12 shows a block diagram of the current controlled three phase inverter simulated in PSIM. A three phase voltage source inverter was connected to a microgrid through a LC filter. The reference current for the current control loop $i_{dq(ref)}$ was provided in the d-q domain. The current feedback i_{dq} was obtained after the Park transformation of the three phase inverter output current i_{abc}.

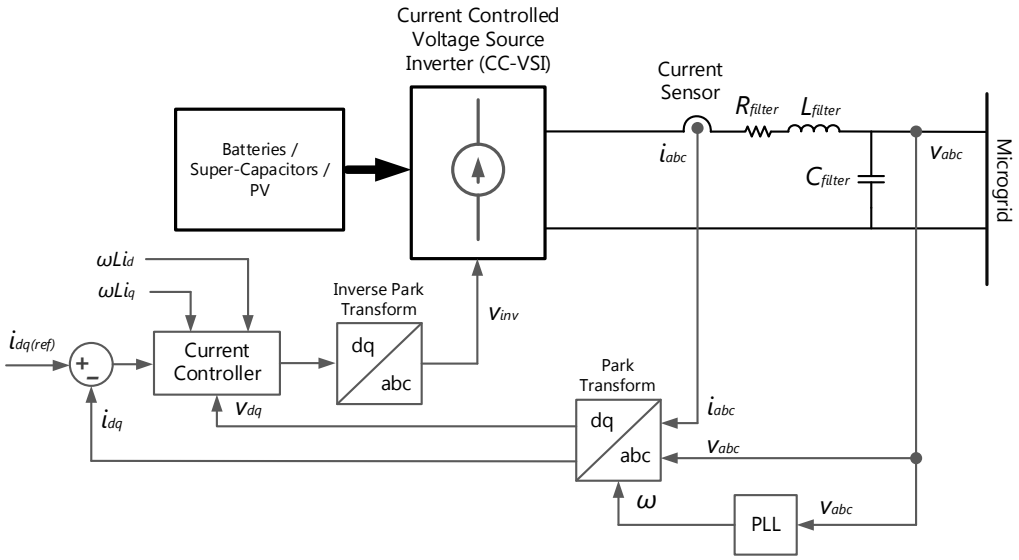

Figure 3.12. Block diagram of current controlled three phase inverter for PSIM simulation.

The voltage feedforward v_{dq} was also provided to the current controller block by transforming the three phase inverter output voltage v_{abc} using the Park transformation. The cross coupling terms, $\omega L i_d$ and $\omega L i_q$ were also fed into the current controller. The phase locked loop (PLL) provides the phase information for the Park transformation and Inverse Park transformation blocks using the microgrid voltage. The control signals generated by

the current controller was then transformed backed into a-b-c domain using the inverse Park transformation which provides the required inverter voltage v_{inv} for exchange of the reference current between the DC source and the microgrid. This voltage was generated by driving the three phase inverter with a gate signal generator.

Figure 3.13 shows the PSIM implementation of the three phase current controlled inverter system. A 400 V_{dc} source was connected through a three phase inverter and a LC filter to a microgrid. The inverter also supplied power to a local load with resistance of 14 ohm per phase. The current and the voltage feedbacks were transformed from the a-b-c domain to d-q domain using the Park transformation and feedback to the current control loop shown in Figure 3.14.

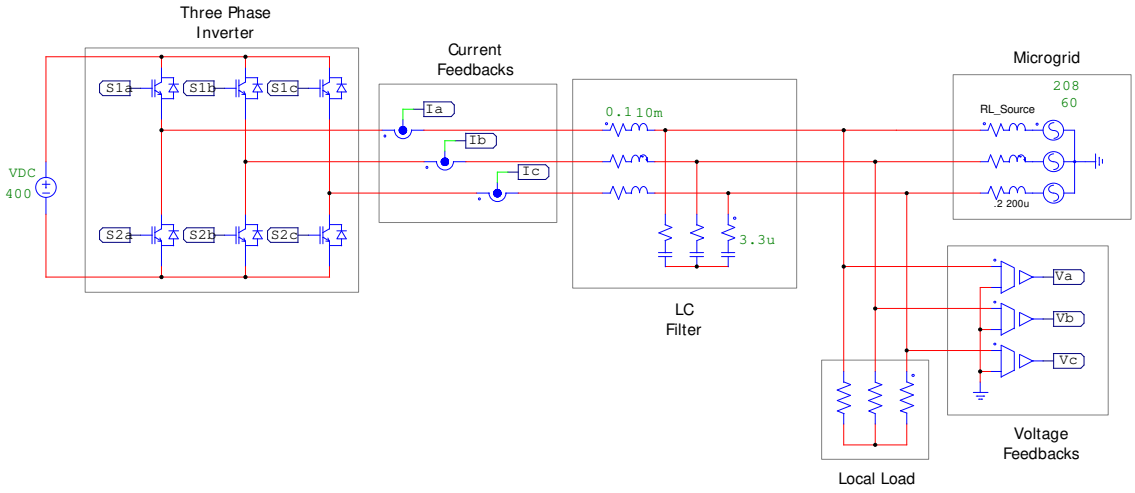

Figure 3.13. PSIM schematic of the implemented current control inverter.

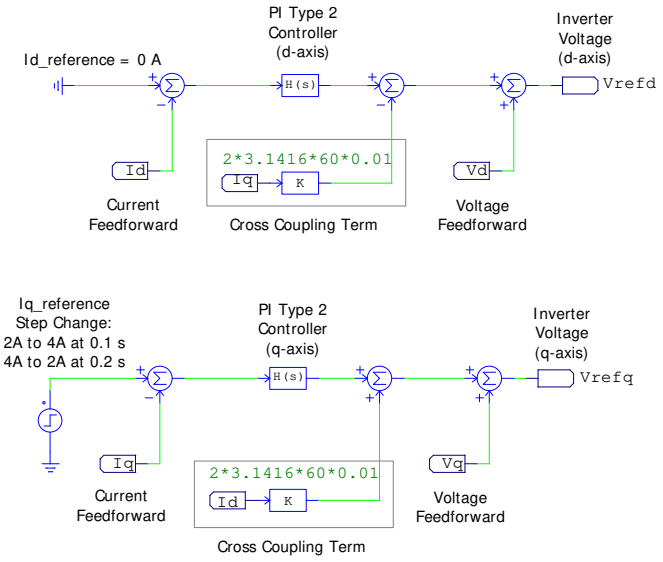

Figure 3.14. d and q axis current controller implementation in PSIM.

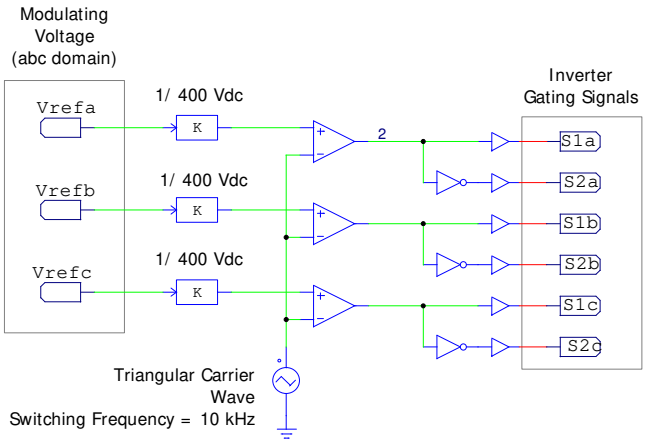

Figure 3.15. Gate signal generation schematic in PSIM.

The $I_{d\_reference}$ current was set to 0A to keep the reactive power at 0. The $I_{q\_reference}$ was set to a step increase from 2 A to 4 A at simulation time of 0.1 s and again to a step decrease from of 4 A to 2 A at simulation time of 0.2 s so that the active power exchange between the DC source and grid could be changed based on the step changes (In PSIM, since the convention for d and q axis components are reversed, the I_q current controls the

active power while the I_q controls the reactive power). The cross coupling terms and the voltage feedforward terms were also added in the current controller. The d and q axis voltages generated by the controller, V_{refd} and V_{refq} was then transformed back into the a-b-c domain using the inverse Park transformation. The reference voltages, V_{refa}, V_{refb} and V_{refc} were fed into the gate signal generation module where it was normalized with respect to the DC side voltage as shown in Figure 3.15. These reference voltages thus are the modulating signals for three phase pulse width modulation. Each reference voltage was compared with a triangular carrier wave with a switching frequency of 10 kHz to generate the gate signals for the three phase inverter.

3.3. Design and implementation of virtual synchronous machine

Using the current controller designed in Section 3.2 along with the virtual synchronous machine algorithm the PV-hydro system with the added VSM was implemented in OPAL-RT real time digital simulation software. The implementation of VSM in the OPAL-RT system along with the procedure to perform transient analysis of the system using software in the loop simulations are presented in this section.

3.3.1. Algorithm for implementation of virtual synchronous machine

The virtual synchronous machine was added to the PV-hydro benchmark microgrid system to reduce the frequency variations in the system due to PV fluctuations and\or load changes. The details of the virtual synchronous machine implemented in the PV–hydro microgrid benchmark system is shown in Figure 3.16. VSYNC's topology described in Section 2.3.2 was used for the implementation. A phase locked loop (PLL)

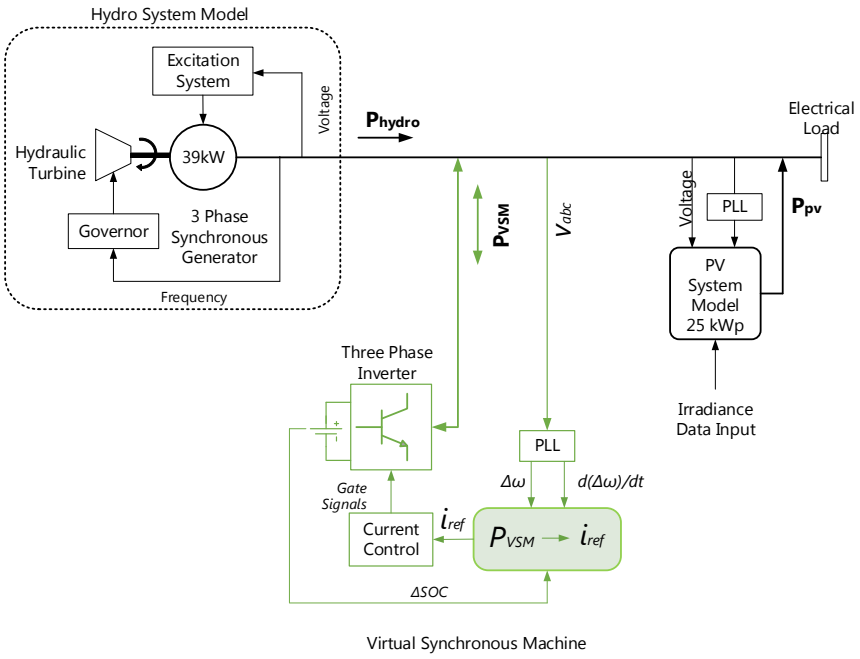

Figure 3.16. Details of the virtual synchronous machine implemented in the benchmark PV-hydro microgrid system.

was used to measure the changes in system frequency along with the rate of change of frequency. Based on these measurements the power P_{VSM} that the virtual synchronous machine needed to exchange with the microgrid system was calculated using Equation (2.27). The inertial constant, K_I, and the damping constant, K_p, was calculated using Equations (2.28) and (2.29) respectively as

$$K_I = \frac{P_{VSM\_NOM}}{(\frac{d\Delta f}{dt})_{max}} = \frac{6400\ W}{0.5\ Hz/s} = 12800 \tag{3.14}$$

$$K_P = \frac{P_{VSM\_NOM}}{(\Delta f)_{max}} = \frac{6400\ W}{2\ Hz} = 3200 \tag{3.15}$$

The nominal power rating of the VSM, P_{VSM_NOM} was taken to be 6400 W which was 10% of the total size of the benchmark PV-hydro system. Using, ISO standards, the maximum allowable frequency deviation was 3 Hz in either direction (±2.5%) and the maximum

allowable ROCOF was 1.2 Hz/s in either direction (± 1%) [39]. The values of $(\frac{d\Delta f}{dt})_{max}$ and $(\Delta f)_{max}$ were selected to be slightly lower at 0.5 Hz/s and 2 Hz respectively.

An additional feedback signal of the change in state of charge of the energy storage device ΔSOC was also added to maintain to the battery state of charge at 50%. The energy storage either absorbed or injected power depending upon whether the state of charge was below or above 50%. Hence, the VSM power Equation of (2.27) was modified to include the state of charge feedback as

$$P_{VSM} = K_I \frac{d(\Delta f)}{dt} + K_I(\Delta f) + K_{SOC}(\Delta SOC) \tag{3.16}$$

where, K_{SOC} is state of charge constant. Hence, the modified equation to calculate the VSM power consisted of three components, the inertial component, the damping component and the state of charge component respectively. The value of state of charge constant, K_{SOC} was selected such that VSM exchanged a maximum power of 2500 W when the SOC deviation was 30% in either direction as

$$K_{SOC} = \frac{2500\ W}{0.3} = 8333.33 \tag{3.17}$$

The reference currents were then set using Equations (2.31) and (2.32) using the calculated power P_{VSM}. Based on the reference current, the current controller block described in Section 3.2.2 and 3.2.3 generates the necessary gate signals for the three phase inverter phase inverter.

3.3.2. Implementation of virtual synchronous machine in OPAL-RT real time digital simulator

Based on the change in frequency and the rate of change in frequency, power was injected or absorbed by the VSM through the three phase inverter to emulate the inertial and damping properties of a real machine. The reduction in frequency variations using the VSM in the PV-hydro microgrid was then studied using OPAL-RT real time digital simulation system which performed software in the loop simulations of the designed system.

Figure 3.17 shows the model of the PV-hydro system with the virtual synchronous machine implemented in OPAL-RT system. The model for benchmark PV-hydro system is the same as described Section 3.1.3 but a virtual synchronous machine was added to the system through the 'VSM Breaker'. The load connected to the system was again a resistive load.

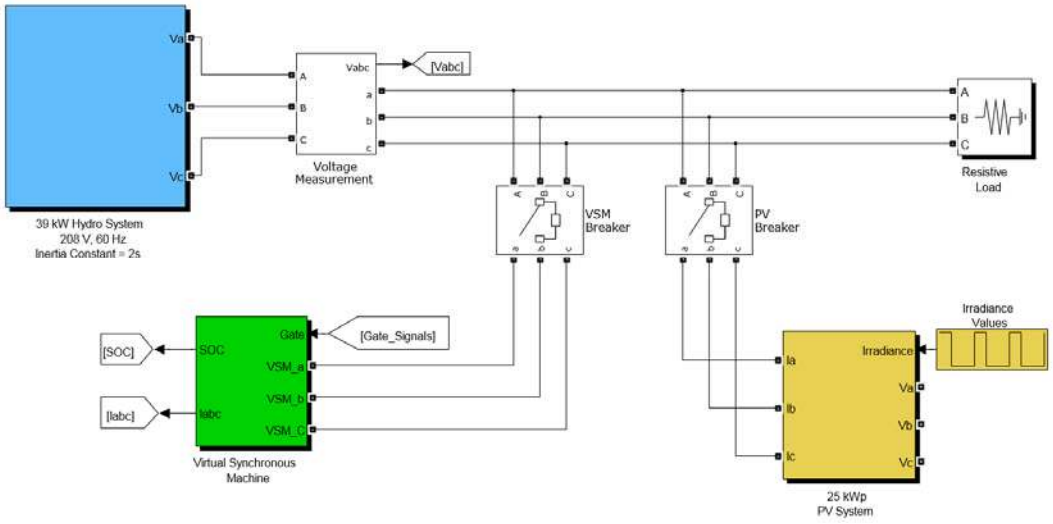

Figure 3.17. Model of PV - hydro system with virtual synchronous machine in OPAL-RT.

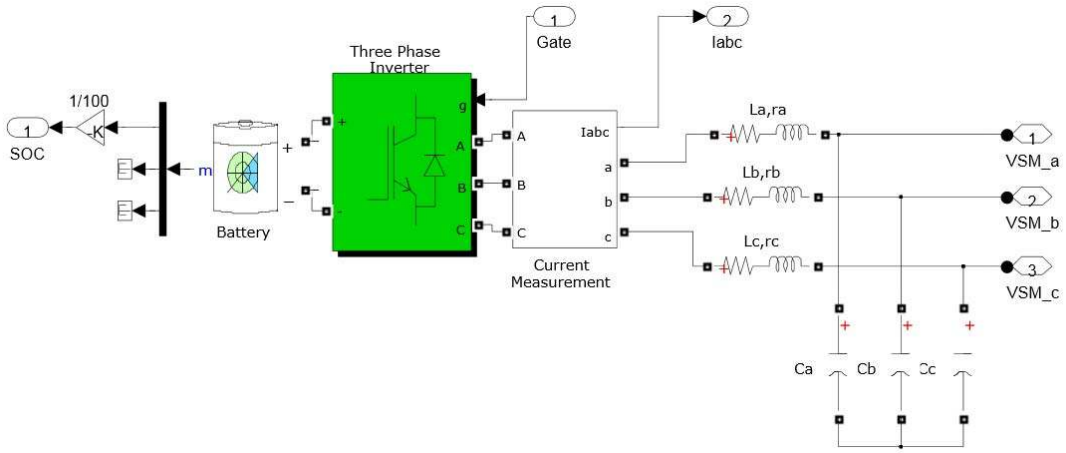

Figure 3.18. Details of the virtual synchronous machine block in OPAL-RT.

The details of the virtual synchronous model block are shown in Figure 3.18. A battery at 400 V_{dc} was connected to a three phase inverter to produce AC power and a LC filter as designed in Section 3.2.1 to produced three phase output of the virtual synchronous machine indicated by the ports VSM_a, VSM_b and VSM_c. Although a 400 V battery was not practically available, it was assumed that this voltage was available through a DC-DC converter for the purpose of this study. The gate signals for inverter was provided by the control circuit which is describe below. The current measurement block provides current feedback to the control circuit. Similarly, the normalized SOC was also a feedback to the control circuit.

Next, the control circuit for the virtual synchronous machine was developed. As shown in Figure 3.19 a three phase PLL was used to calculate the phase information using the microgrid voltage V_{abc}. The sine and cosine of the phase was then fed into the Park transformation block to obtain the d-q components of the microgrid voltage V_{abc} and VSM output current I_{abc}.

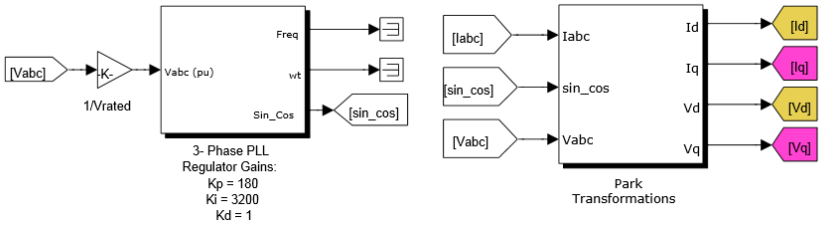

Figure 3.19. Implementation of three phase PLL and Park transformations in OPAL-RT.

The d-q coordinate voltages, V_d and V_q into the VSM algorithm block to generate the reference d-axis current I_{d_ref} as shown in Figure 3.20. Other inputs to the VSM algorithm block were the SOC of the battery, microgrid voltage V_{abc}, required SOC of 0.5 and rated frequency of 60 Hz. The details of the VSM algorithm block is shown in Figure 3.21.

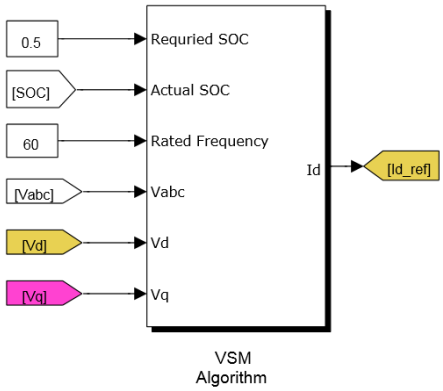

Figure 3.20. VSM algorithm block in OPAL-RT.

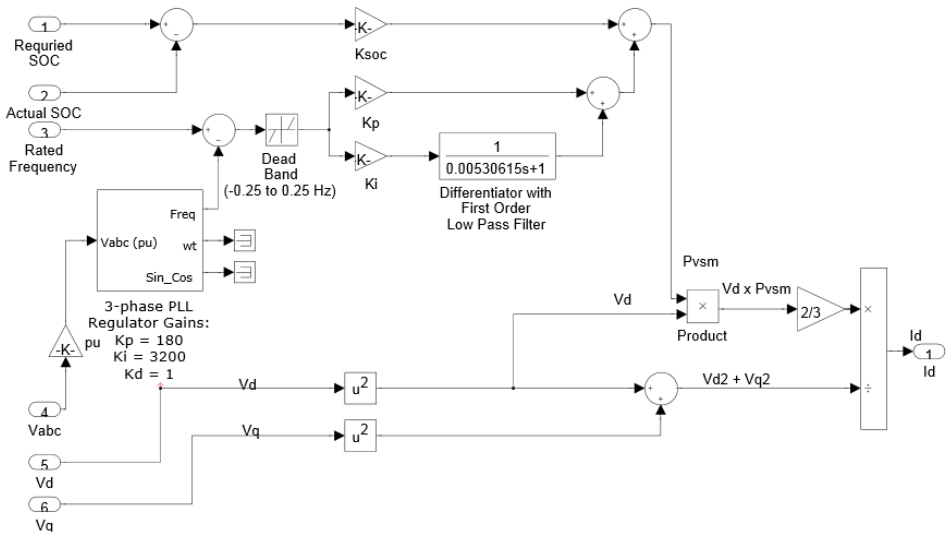

Figure 3.21. Details of VSM algorithm implemented in OPAL-RT.

The frequency of the PV-hydro system was measured using the three phase PLL. The frequency of the system was then compared with the rated frequency to obtain the change in frequency. Using the change in frequency the ROCOF was calculated using derivative with a first order low pass filter. The cut-off frequency of low pass filter was set to 30 Hz. This equivalent to measuring the ROCOF of the system every two cycles [40]. To calculate the VSM power as described in Equation (3.16) the change in frequency was multiplied by the constant $K_P = 3200$ and the ROCOF by the constant $K_I = 12800$. Similarly, the SOC of the battery was compared with the rated SOC to obtain the change in SOC which was multiplied by the constant $K_{SOC} = 8333.33$. The product of all these quantities was added to obtain the VSM power P_{VSM}. Once, the VSM power was calculated the reference d-axis current for the current controller was obtained based in Equation (2.31) using V_d and V_q.

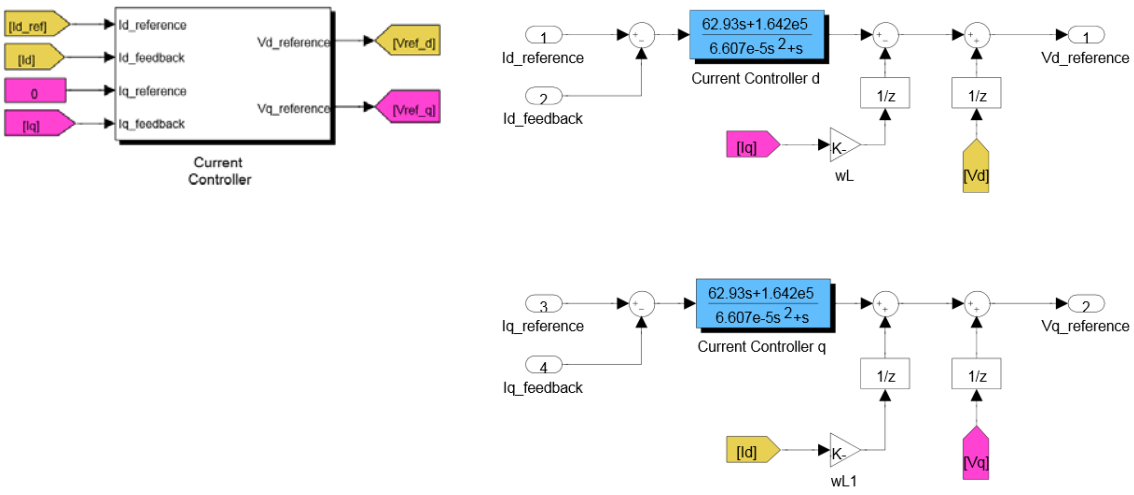

Figure 3.22. Current controller implementation in OPAL-RT.

The reference current was then fed into the current controller block as shown in Figure 3.22. The I_d and I_q VSM output currents were the feedback signals of the current controller. The details of the current controller block is also shown in Figure 3.22. The current control topology was exactly the same as described in Section 2.2.4. Unit delays were added to the cross- coupling terms and the voltage feedforward to prevent the formation of algebraic loops which would slow the simulations considerably. The current controller generates the reference inverter voltages $V_{d\_reference}$ and $V_{q\_reference}$ in the dq domain.

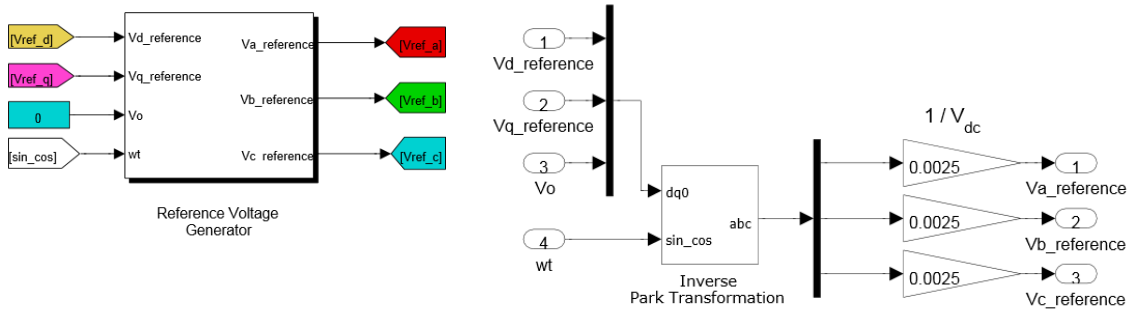

Figure 3.23. Reference voltage generator in OPAL-RT.

These reference inverter voltages were fed into the reference voltage generator as shown in Figure 3.23 which generated the inverter reference voltages in the a-b-c domain by performing an inverse park transformation. The voltages were then normalized to the DC side voltage of the inverter. The reference voltages in the a-b-c domain were finally passed into the gate signal generator to generate the gating signals. The gate signal generator produced the gating signals with the reference voltages as the modulating signals at a switching frequency 10 kHz as shown in Figure 3.24. These gate signals drive the three phase inverter of the virtual synchronous machine model shown in Figure 3.19.

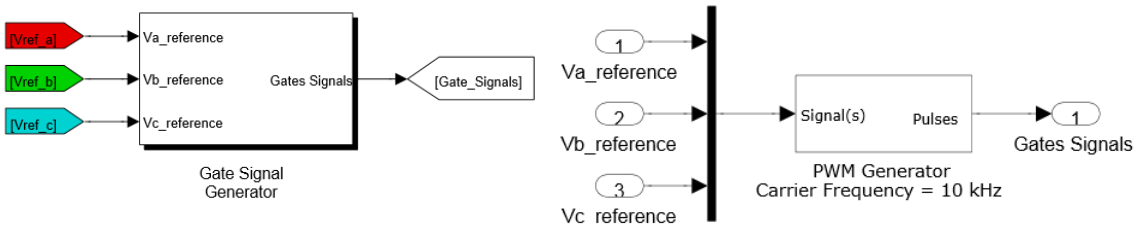

Figure 3.24. Gate signal generator implementation in OPAL-RT.

The frequency variations in the PV-hydro system with and without the VSM were then compared.

CHAPTER 4 RESULTS AND ANALYSIS

Chapter 4 presents results and analysis from the developed PV-hydro benchmark. The frequency variations in the PV-hydro benchmark microgrid due to irradiance changes are presented. Similarly, the simulation results of the designed current controller in PSIM simulation software are also presented. Finally, the reduction in frequency variations in system with the addition of the virtual synchronous machine are shown through software in the loop simulations performed in OPAL-RT real time digital simulation system.

4.1. PV-Hydro microgrid benchmark

The frequency variations and the ROCOF in the PV-hydro microgrid benchmark system due step irradiance changes and a real irradiance pattern are presented in this section. The effect of frequency variations on the operation and stability of the system are also discussed.

4.1.1. Frequency variations in hydro only system due to step load changes

Figure 4.1 shows the frequency variations in the 39 kW hydro system due to step increase in load of 2 kW, 4 kW and 6 kW. The frequency deviation from the rated value of 60 Hz increased with the increase in the step load as expected. The minimum frequency for 2 kW, 4 kW and 6 kW step increase were 59.27 Hz, 58.52 Hz and 57.62 Hz respectively. However, the time required for the frequency to return to 60 Hz was almost the same for all the three cases.

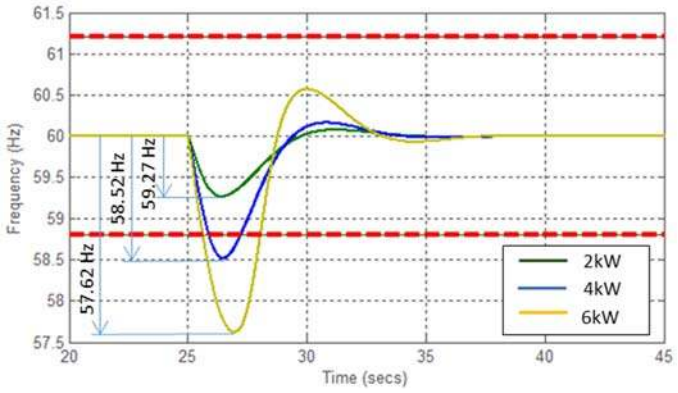

Figure 4.1. Frequency variation of 39 kW hydro system for step load changes of 2 kW, 4 kW and 6kW.

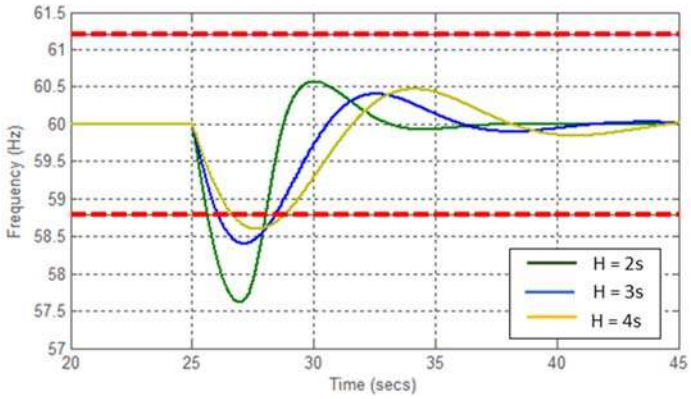

Figure 4.2. Frequency variation of 39 kW hydro system for different inertia constant of 2 s, 3 s and 4s.

Figure 4.2 shows the frequency variation in the 39 kW hydro system for a step load increase of 6 kW but at different inertia constants of 2 s, 3 s and 4s. With increase in the inertia constant the frequency deviations were reduced but on the other hand the response of the system became slower, as it took a longer time for frequency to return to the rated value with the higher inertia constant.

4.1.2. PV power output at different irradiance levels

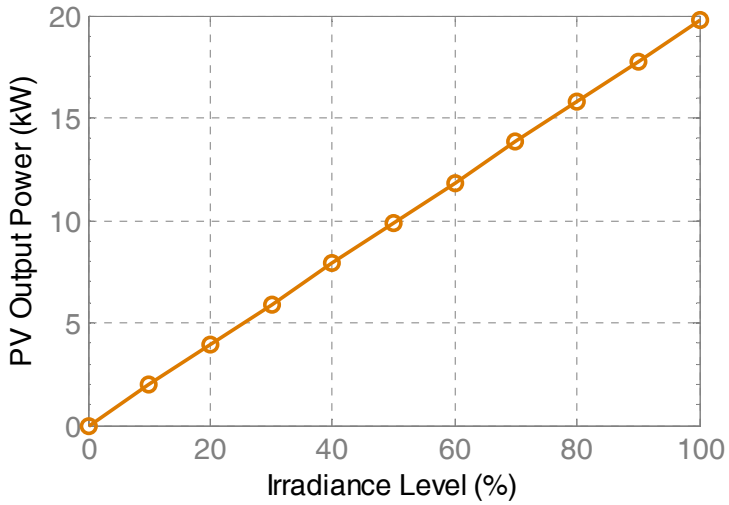

Figure 4.3. Output power from 25 kWp PV system model for different irradiance levels.

Figure 4.3 shows the output power from the 25 kWp PV model at different irradiance values. The output power from the PV model at difference irradiance levels of 25%, 50%, 75% and 100% (normalized to 1000 W/m^2) are shown. It is clear that the power output increased linearly with increase in the irradiance input. However, the output power was slightly lower than the rated value of PV system as the actual output power was de-rated by the efficiency of the system which was set at 96.5%.

4.1.3. Frequency variations in PV-hydro system due step change in irradiance pattern and real irradiance patterns

Figure 4.4 (a) shows a step change in input irradiance to the 25 kWp PV model from 750 W/m^2 to 250 W/m^2. The frequency variations in the PV-hydro system due to this step change in irradiance are shown in Figure 4.4(b). The frequency deviated outside the recommended operating range of ± 2.5% but stayed within the critical operating range of ±15%.

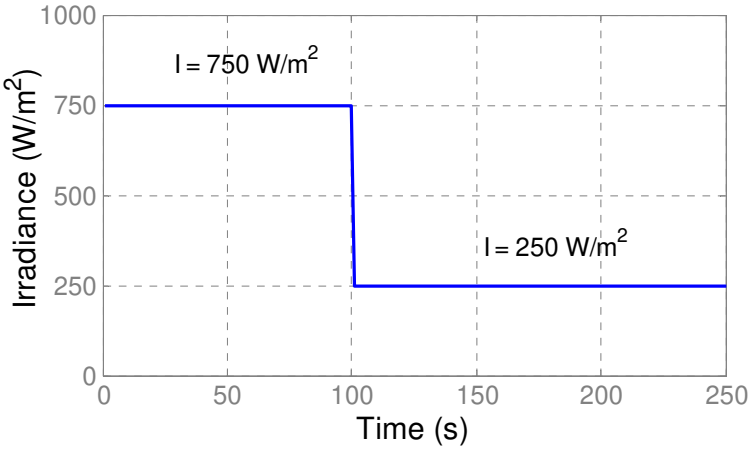

(a)

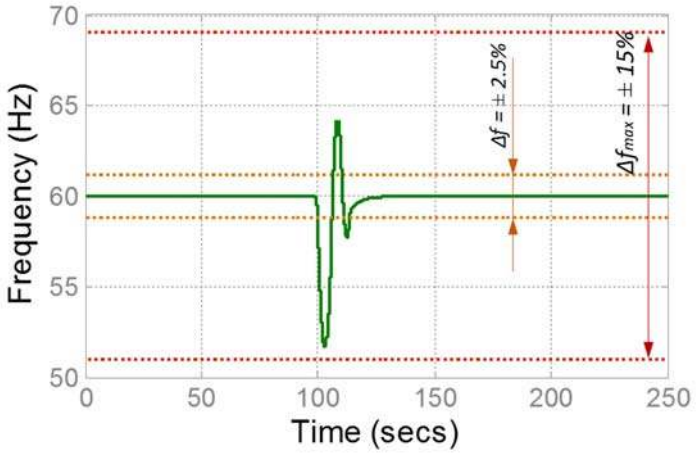

(b)

Figure 4.4. (a) Step change in input irradiance from 750W/m^2 to 250 W/m^2.

(b) Frequency variations in the PV-hydro benchmark system due to step change in irradiance from 750 W/m^2 to 250 W/m^2.

Figure 4.5 shows a more detailed view of the frequency variations from a simulation time of 80s to 130s. The minimum value to which the frequency deviated was 51.69 Hz and the

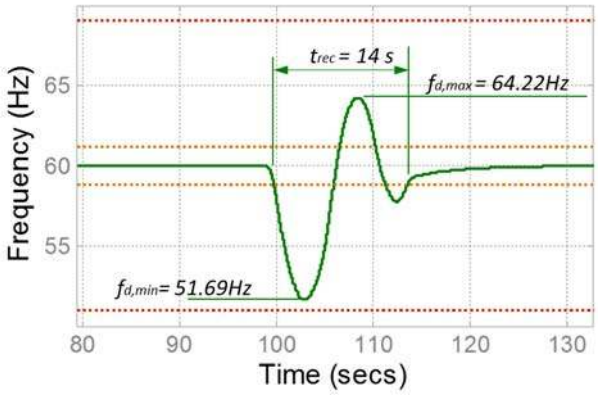

Figure 4.5. Detailed view of frequency variations in the PV-hydro benchmark system due to step change in irradiance from 750 W/m^2 to 250 W/m^2.

maximum value to which the frequency deviated was 64.22 Hz, both of which were outside the recommended operating range of ±2.5%. Moreover, the recovery time, which is the time required for the frequency to return within the recommended ±2.5% band, was 14 s which was higher than the recommended limit of 10 s as per ISO 8528-5 standard for generating sets. Moreover, the maximum value of ROCOF in the system was 8.2 Hz/s as shown in Figure 4.6 well over the recommended limit of 0.6 Hz/s.

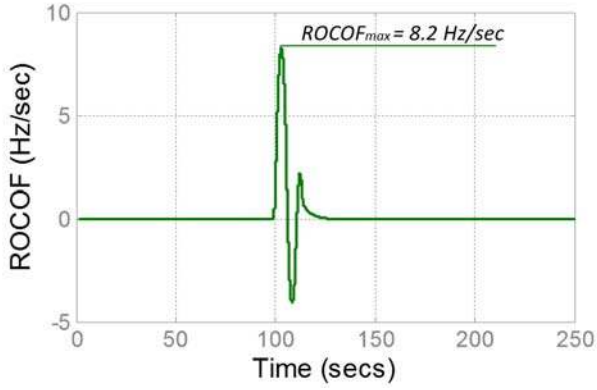

Figure 4.6. ROCOF in the PV-hydro benchmark system due to step change in irradiance from 750 W/m^2 to 250 W/m^2.

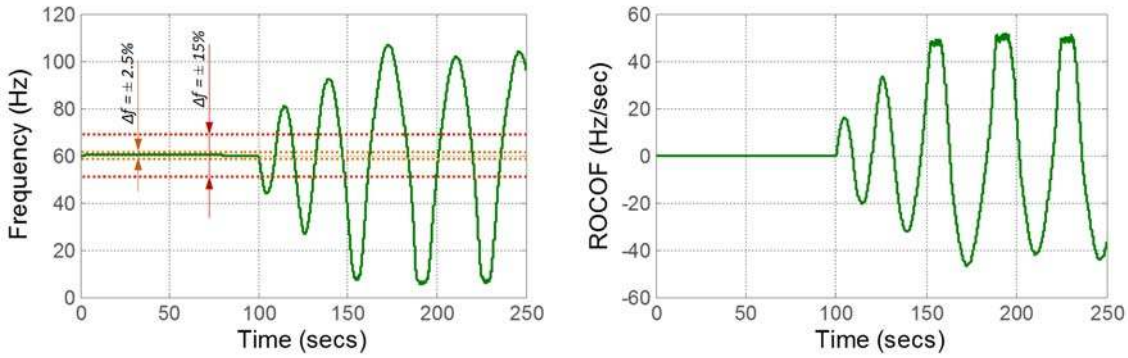

(a) (b)

Figure 4.7. (a) Frequency variations in the PV-hydro benchmark system. (b) ROCOF due to step change in irradiance from 950 W/m^2 to 250 W/m^2.

Figure 4.7 (a) and Figure 4.7 (b) show the frequency variations and the ROCOF respectively in the PV-hydro benchmark system for a step change in irradiance from 950 W/m^2 to 250 W/m^2. With the higher step change the corresponding frequency variations were significantly higher compared to the previous case of step change in irradiance from 750 W/m^2 to 250 W/m^2. In addition, the system frequency no longer returned to the steady state and the PV-hydro system showed sustained oscillations. The same was true for the ROCOF as well, very high value of ROCOF was observed which would cause the relays in the system to trip.

Figure 4.8 (a) shows a plot of 250 second snapshot of real irradiance data obtained from the microgrid lab in SDSU as described in Section 3.1.3. Figure 4.8 (b) shows the frequency variations in the benchmark PV-hydro system due to this irradiance pattern for different PV system size of 10 kWp, 15 kWp and 25 kWp. In all the three cases, the

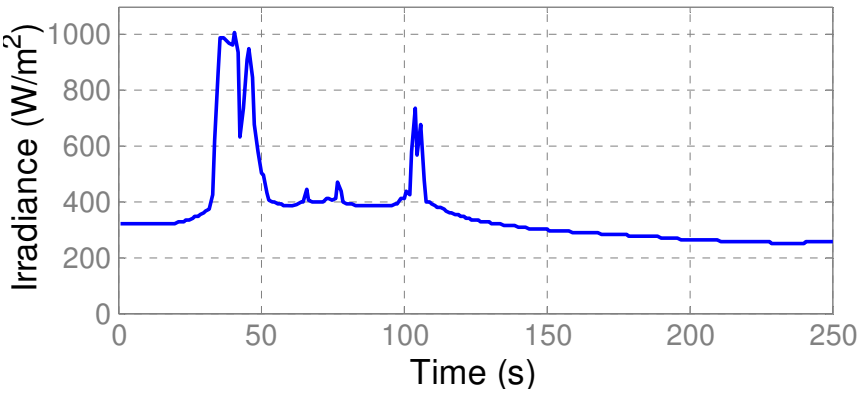

(a)

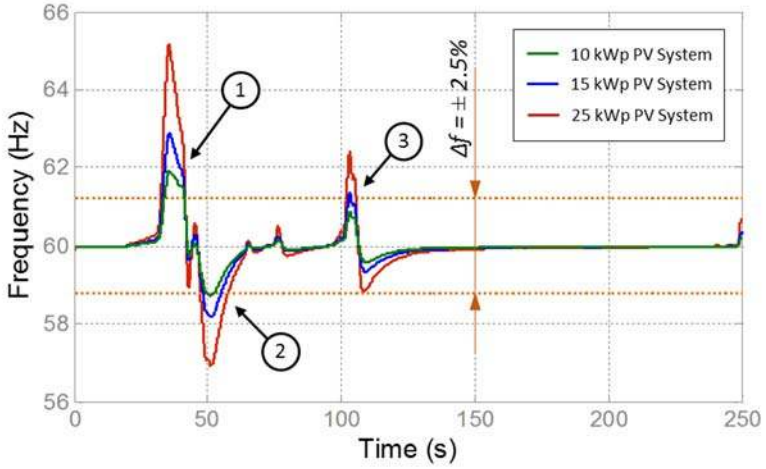

(b)

Figure 4.8. (a) 250 second snapshot of real irradiance data obtained from microgrid lab in SDSU (Sampling time = 1 s). (b) Frequency variations in the benchmark PV-hydro system due to real irradiance data for 10, 15 and 25 kWp PV system.

frequency of the system went out of the recommended operating range of ±2.5%. However, with increase in the PV system size the magnitude of the frequency variations also increased proportionately as expected. The maximum and the minimum value of frequency deviation above and below the rated frequency of 60 Hz are summarized in Table 4.1.

Table 4.1. Maximum and minimum value of frequency deviation above and below the rated 60 Hz frequency in PV-hydro benchmark system due to real irradiance changes.

PV system size	Maximum value of frequency deviation above 60 Hz	Minimum value of frequency deviation below 60 Hz
10 kWp	61 .92 Hz	58.74 Hz
15 kWp	62.86 Hz	58.17 Hz
25 kWp	65.13 Hz	56.93 Hz

The recovery time of the frequency at three different instances when the frequency went out of the recommended operating range of ±2.5% as marked in Figure 4.8 (b) is listed in Table 4.2. In most cases the recovery time was within the recommended 10 s limit except for instance 2 when 25 kWp PV system is connected to the PV-hydro benchmark system where the recovery time was slightly over the 10 s limit.

Table 4.2. Frequency recovery time at different instances in the simulation of PV-hydro system with real irradiance changes.

PV system size	Recovery time for instance 1	Recovery time for instance 2	Recovery time for instance 3
10 kWp	7.41 s	3.38 s	N/A
15 kWp	8.05 s	7.20 s	0.90 s
25 kWp	8.76 s	10.41 s	3.60 s

Figure 4.9 shows the ROCOF in the PV-hydro benchmark system due to the real irradiance pattern shown in Figure 4.8(a) for different PV system sizes of 10, 15 and 25 kWp. The maximum values of the ROCOF for different size of PV system are summarized in Table 4.3. In all three cases, the ROCOF was well over the recommended limit of 0.6 Hz/s. Hence, virtual synchronous machine was used to reduce the ROCOF within recommended limits while maintaining same penetration levels.

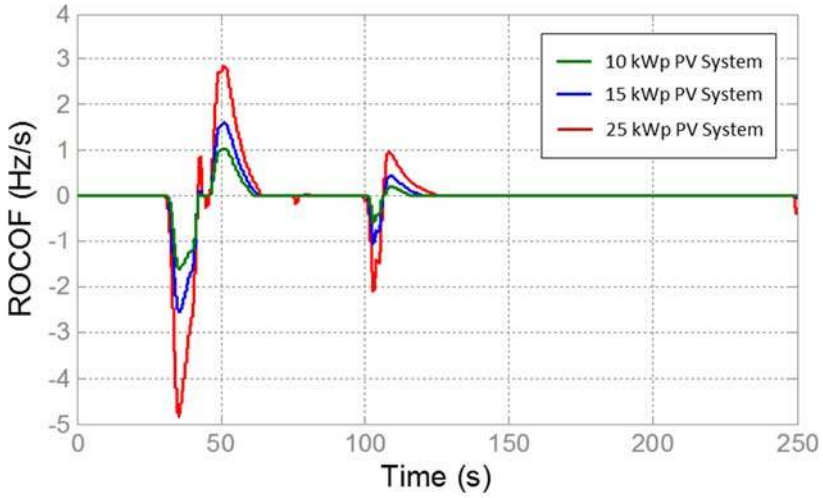

Figure 4.9. ROCOF in the PV-hydro benchmark system due to real irradiance changes for different PV system sizes of 10, 15 and 25 kWp.

Table 4.3. Maximum value of ROCOF in the benchmark PV-hydro system due to real irradiance changes.

PV System Size	**Maximum value of ROCOF**
10 kWp	1. 62 Hz/s
15 kWp	2.57 Hz/s
25 kWp	4.83 Hz/s

4.2. Current controlled three phase voltage source inverter

The frequency response of the designed LC filter is presented in this section. The results obtained from design and testing of the current controller transfer function designed in Section 3.2 is also described.

4.2.1. Frequency response of LC filter

The filter design for the three phase voltage source inverter is shown in Figure 4.10 (a). The inductance and capacitance were 10 mH and 2.60 µF using Equations (3.4) and (3.5). The values used were 10 mH and 3.3 µF respectively which were the standard values available commercially. The frequency response of the designed LC filter shown in Figure 4.10 (b) had a cutoff frequency of 876.12 Hz which was a decade below the switching frequency of 10 kHz. This ensured that the LC filter provided adequate filtering to the high frequency switching noise and allowed the low frequency signals to pass through.

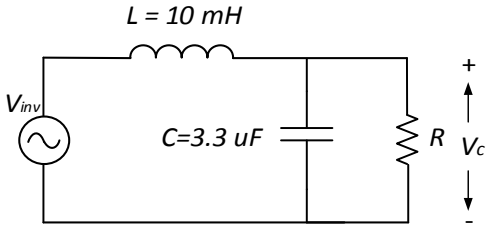

(a)

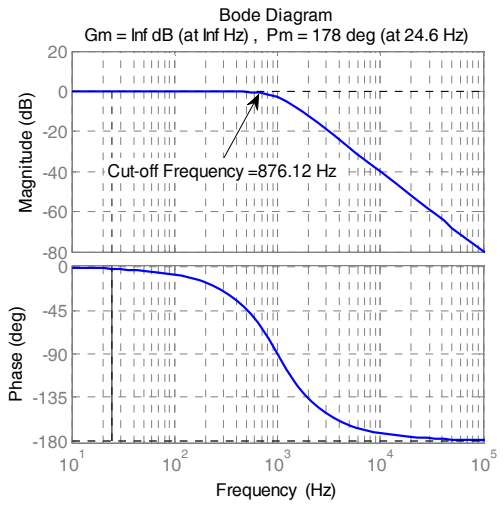

(b)

Figure 4.10. (a) LC filter. (b) Frequency response of the LC filter.

4.2.2. Frequency response and step response of current controller

The transfer function of the plant, $G_{plant(s)}$, for the design of the current controller based on the inductance and capacitance value was

$$G_{plant}(s) = \frac{I_L(s)}{V_{inv}(s)} = \frac{100}{s + 10} \tag{4.1}$$

The frequency response of the plant is shown in Figure 4.11. The plant had an infinite gain margin and a phase margin of 95.7 degrees at 15.8 Hz.

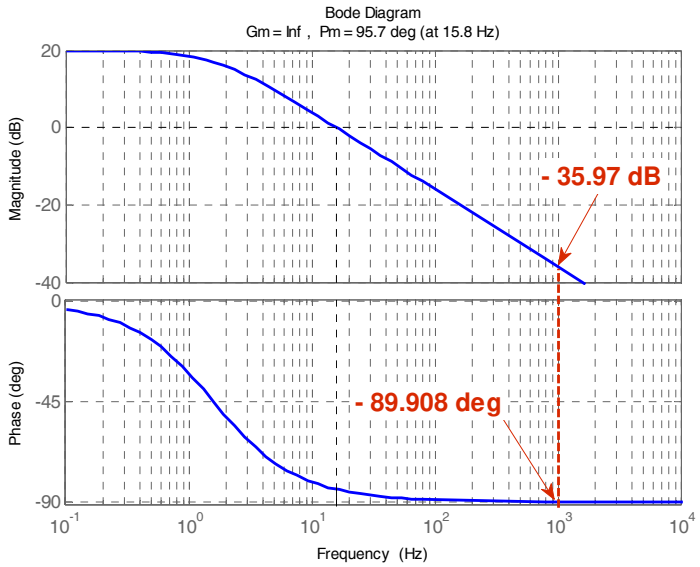

Figure 4.11. Frequency response of the plant for the current controller.

The magnitude, $|G_{plant}(\omega_x)|$, and the phase $\angle G_{plant}(\omega_x)$, of the plant at desired cross-over frequency of 1 kHz was found from Figure 4.11 as

$$\left|G_{plant}(\omega_x)\right| = 0.0159 = -35.97\ dB \tag{4.2}$$

$$\angle G_{plant}(\omega_x) = -89.908° \tag{4.3}$$

The parameters for the design of the PI type 2 controller are summarized in Table 4.4.

Table 4.4. Parameters for design of PI type 2 controller.

Parameter	Value
θ_{boost}	44.908°
K	2.408
τ	383.24 µs
T_p	66.09 µs
K_{PI}	62.93

Substituting the parameters in Table 4.4 into Equation (3.7) yields the transfer function of the PI type 2 controller, $C_{PI2}(s)$, as

$$C_{PI2}(s) = \frac{62.93s + 1.642e^{05}}{6.609e^{-05}s^2 + s} \tag{4.4}$$

The transfer function was incorporated into the closed loop current control system of the three phase inverter as shown in Figure 4.12.

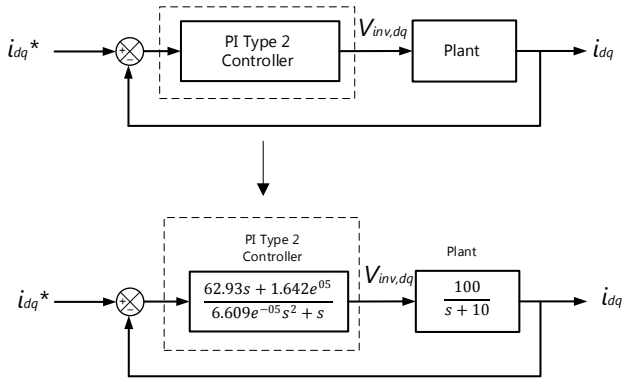

Figure 4.12. Closed loop current control system with PI type 2 controller.

Figure 4.13 shows the frequency response of the plant and the PI type 2 current controller. In the magnitude the plot, the controller had a high gain with a slope of -20 dB/decade at lower frequency range which reduced the steady state error of the closed loop system. The slope was reduced to 0 dB/dec at f_1=415.15 Hz (corresponding to the time constant τ) and then back to -20 dB/dec at f_2=2411.14 Hz (corresponding to the time constant T_p) at higher frequency range. The gain was lower at higher frequency which insured attenuation of high frequency switching noises. Moreover, in the phase plot, the controller added phase of 45.09° to bring the phase margin of the loop transfer function of the combined plant and the current controller to 45° at the cross-over frequency as per the design specifications. Figure 4.14 shows the frequency response of the loop transfer function of the combined plant and the designed PI type 2 controller combined. The loop transfer function of the system had a phase margin of 45° at crossover frequency of 1 kHz which matched the design specifications described in Section 3.2.2.

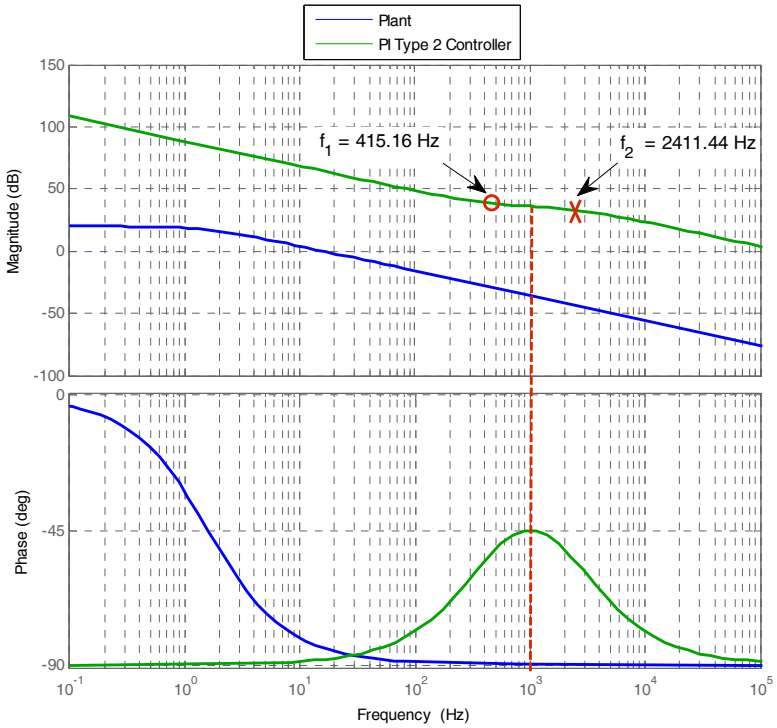

Figure 4.13. Frequency response of the plant and the current controller.

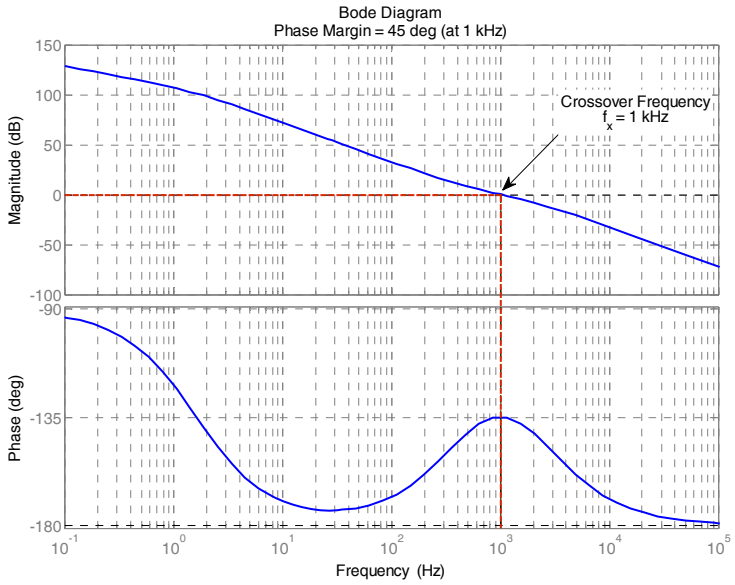

Figure 4.14. Frequency response of the combined loop transfer function of the plant and PI type 2 controller.

Figure 4.15 shows the step response of the closed loop current control system which had an overshoot of 33.5%, an acceptable value for inverter system. Also, the settling time of 0.98 ms indicated that the controller responded fast enough to changes in the reference signal.

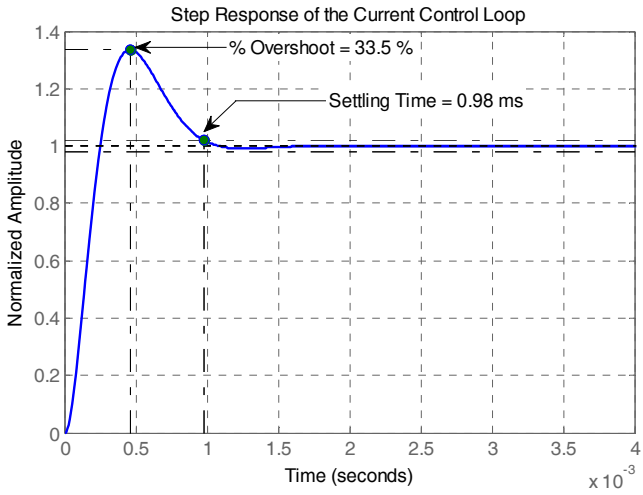

Figure 4.15. Step response of the closed loop current control system.

4.2.3. Simulation of control of output current and power of three phase inverter

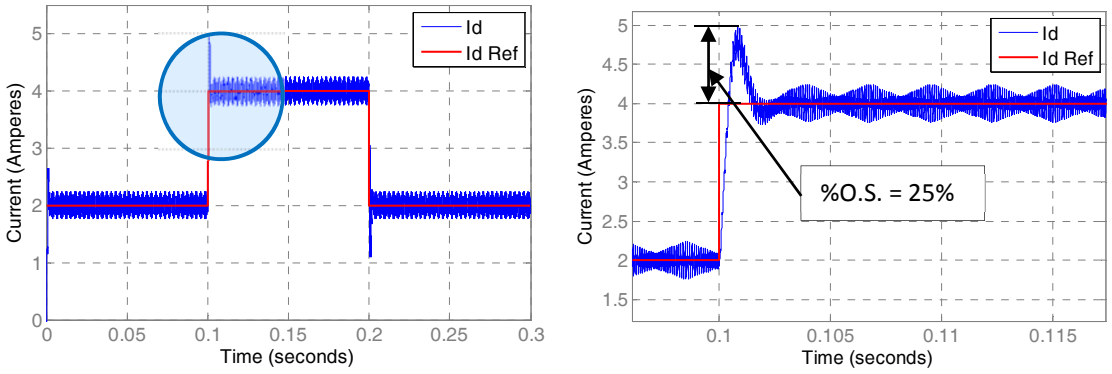

(a) (b)

Figure 4.16. (a) Step changes in reference d-axis current and actual d-axis current.

(b) Detailed view of the d-axis current response a simulation time of 0.1 s.

Figure 4.16(a) shows a step change in the d-axis reference current from 2 A to 4 A and back to 2 A in the current-controlled-voltage-source inverter simulated in the PSIM simulation software as described in Section 3.2.3. The actual current I_d tracked the reference current I_{d_ref} well. The ripple in the output current was attributed to the electromagnetic noise due to the fast switching of the inverter switches. Figure 4.16(b) shows a detailed view of the circled section in Figure 4.16 (a). There was an overshoot of 25% in the current response before the d-axis current settled to the new value of 4 A. The overshoot was slightly higher than the expected overshoot of 20% as described in the design of the current controller in Section 3.2.2. This was again due to the electromagnetic noise.

Figure 4.17 shows the output current of the three phase current controlled inverter in the a-b-c domain. As the d-axis current changed from 2 A to 4 A at a simulation time of 0.1 s and down to 2 A at 0.2 s, the peak value of the a-b-c phase currents also changed from 2 A to 4 A at 0.1 s and down to 2 A at 0.2 s. The output current of the inverter was sinusoidal. With the change in the d-axis current, the active power output also changed from 500 W to 1000 W at 0.1 s and again back to 500 W at 0.2 s as shown in Figure 4.18. Since, there was an overshoot in the d-axis current, a similar overshoot was observed in the active power output of the inverter as well.

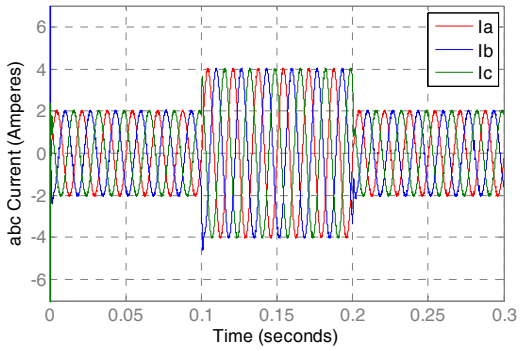

Figure 4.17. Change in output current of the current controlled three phase inverter.

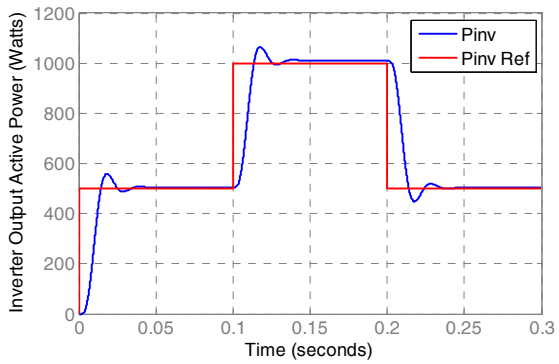

Figure 4.18. Change in output power of the current controlled three phase inverter.

4.3. PV-Hydro benchmark system with addition of VSM

The reduction in the frequency variations and the ROCOF in the PV-hydro benchmark system due to step irradiance change and real irradiance changes due to emulation of virtual inertia by the VSM are presented. This is followed by an analysis of the power and the energy requirements for the implementation of VSM.

4.3.1. Reduction in frequency variations in hydro only system due to step irradiance change

Figure 4.19 shows the reduction in frequency variation in the PV-hydro benchmark system with and without the VSM for a step change in irradiance from

750 W/m^2 to 250 W/m^2. Figure 4.20 shows a more detailed view for a simulation time of 100 s to 180 s. The frequency variation with the VSM was reduced to within the permissible limit of ±2.5% with addition of VSM. The minimum frequency deviation in the PV-hydro system was reduced from 51.69 Hz to 59.15 Hz and there was not overshoot of frequency over the rated value of 60 Hz.

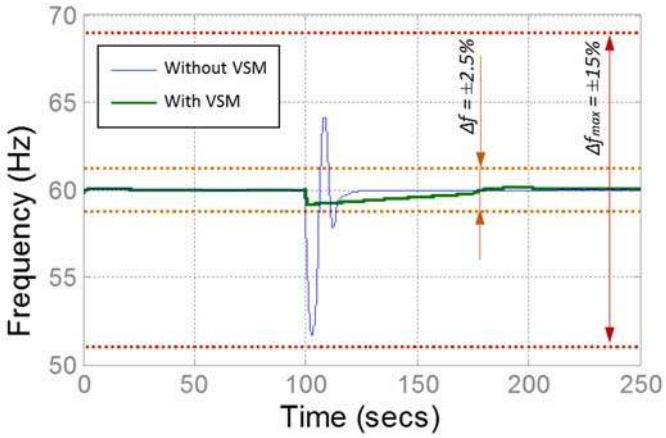

Figure 4.19. Frequency variations in the PV-hydro benchmark system with and without the VSM for step change in irradiance from 750 W/m^2 to 250 W/m^2.

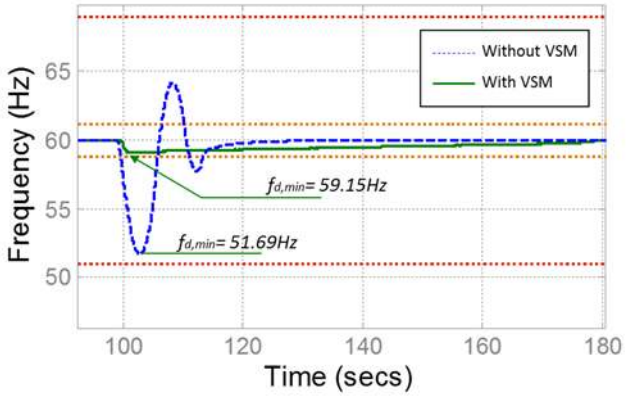

Figure 4.20. Detailed view of frequency variations in the PV-hydro benchmark system with and without VSM for step change in irradiance from 750 W/m^2 to 250 W/m^2.

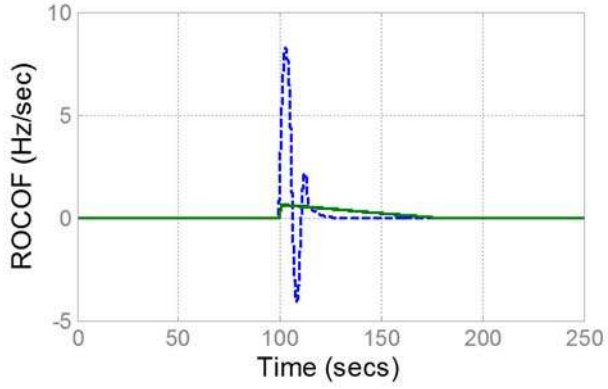

Figure 4.21. ROCOF in the PV-hydro benchmark system with and without VSM for step change in irradiance from 750 W/m^2 to 250 W/m^2.

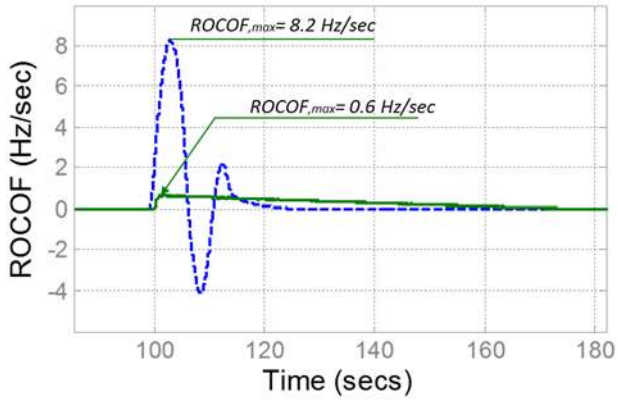

Figure 4.22. Detail view of ROCOF in the PV-hydro benchmark system with and without VSM for step change in irradiance from 750 W/m^2 to 250 W/m^2.

Figure 4.21 shows the reduction in the ROCOF of the benchmark PV-hydro system with the addition of VSM when there was a step change in input irradiance from 750 W/m^2 to 250 W/m^2. Figure 4.22 shows a detailed view of the ROCOF in the PV–hydro system. The maximum value of ROCOF was reduced from 8.2 Hz/s to 0.6 Hz/s. This reduction should avoid the frequency relays from tripping. With the addition of the VSM the ROCOF of the PV-hydro benchmark system for a step change in irradiance from 750 W/m^2 to 250 W/m^2 was reduced by 92.6%.

4.3.2. Reduction in frequency variations in PV-hydro benchmark system due real irradiance changes

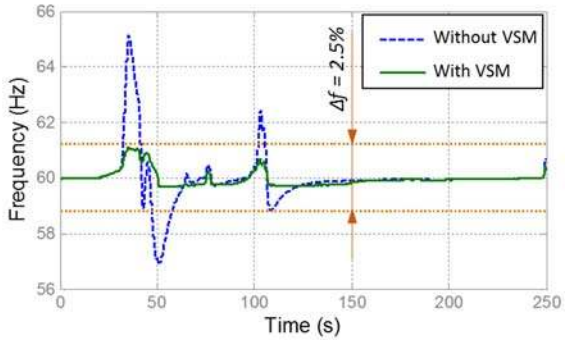

Figure 4.23. Reduction in frequency variations due to real irradiance changes in the PV-hydro benchmark system with addition of VSM.

Figure 4.23 shows the reduction in frequency variations in the PV-hydro benchmark system due to real irradiance changes described in Section 3.1.3 with the addition of VSM. The system frequency now stayed within the normal operating range of ±2.5%. The maximum value of frequency excursion was reduced by 6.3 % and the minimum value of frequency excursion was reduced by 4.7% compared to the case without the VSM. Similarly, Figure 4.24 shows the reduction in ROCOF of the PV-hydro benchmark system with addition of VSM. The maximum value of ROCOF was reduced by 85.4% with the addition of VSM.

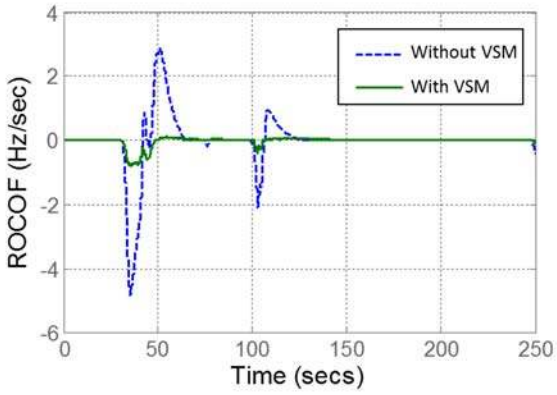

Figure 4.24. Reduction in ROCOF due to real irradiance changes in the PV-hydro benchmark system with addition of VSM.

Figure 4.25 shows that inertia emulated by the VSM in terms of the inertia constant normalized to the size of 39 kW hydro power. The total inertia that could be emulated by the VSM was about 10 s. The actual inertia emulated varied based on the power imbalance in the PV-hydro microgrid system. Figure 4.26. shows as the size of the PV system increased the inertia emulated by the VSM also increased linearly.

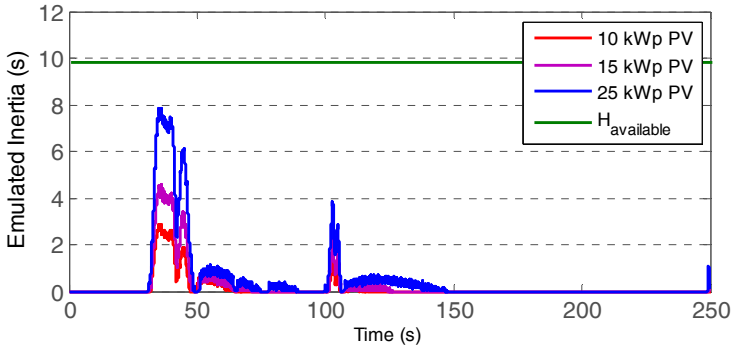

Figure 4.25. Inertia emulated by the VSM for different PV system sizes.

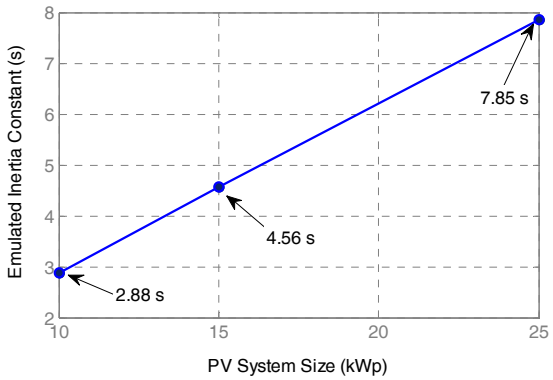

Figure 4.26. Emulated inertia constant vs. PV system size.

The results in Section 4.3.1 and Section 4.3.2 indicate that the addition of VSM makes the integration of 25 kWp PV system into the hydro system possible by maintaining and improving its transient stability. The reduction in frequency variations with addition of VSM for different PV system sizes of 10 kWp, 15 kWp and 25 kWp are summarized in Table 4.5. In all three case, with addition of VSM of maximum and minimum frequency deviation in the system were brought down within the recommended limits of ±2.5% (58.5 – 61.5 Hz). Similarly, the reduction in ROCOF with addition of VSM for different PV system sizes of 10 kWp, 15 kWp and 25 kWp are summarized in Table 4.6. In all three cases, with addition of VSM the peak value of ROCOF in the system was substantially reduced. For the 10 kWp and 15 kWp PV system sizes, the peak value of ROCOF was 0.2 Hz/ and 0.4 Hz/s well within the prescribed limit of 0.6 H/s. For the 25 kWp PV system, the ROCOF was 0.7 Hz/s which was slightly over the prescribed limit of 0.6 Hz/s but should still be tolerable for the frequency relays.

Table 4.5. Maximum and minimum frequency deviations in the PV-hydro system with and without VSM for various PV system sizes.

PV System Size	Without VSM		With VSM	
	Maximum Frequency	**Minimum Frequency**	**Maximum Frequency**	**Minimum Frequency**
10 kWp	61.8 Hz	58.7 Hz	60.5 Hz	59.7 Hz
15 kWp	62.8 Hz	58.1 Hz	60.7 Hz	59.7 Hz
25 kWp	65.1 Hz	56.9 Hz	61.0 Hz	59.6 Hz

Table 4.6. Maximum and minimum value of ROCOF in the PV-hydro system with and without VSM for various PV system sizes.

PV System Size	Maximum ROCOF without VSM	Maximum ROCOF with VSM
10 kWp	1.6 Hz/s	0.2 Hz/s
15 kWp	2.5 Hz/s	0.4 Hz/s
25 kWp	4.8 Hz/s	0.7 Hz

4.3.3. VSM power and energy requirements

Figure 4.27 shows the power that the VSM exchanged with the PV-hydro benchmark microgrid system when there was a step change in input irradiance from 750 W/m^2 to 250 W/m^2. Initially, the power was injected by the VSM into the PV-hydro microgrid to compensate the step change in input irradiance. This caused the SOC of the battery to go below the set value of 50%. Thus at a simulation time of 145 s the VSM

instead started absorbing power from the PV-hydro system to bring the SOC of the battery back to 50%. This was the effect of the added SOC control mechanism described in Section 3.3.1. The peak power handled by the VSM was quite high at 10.10 kW compared to the overall system size of 64 kW (39 kW hydro system and 25 kWp PV system). The net energy that the VSM exchanged with PV-hydro benchmark microgrid system was 11.7 Wh. The net energy was obtained by integrating the area under the curve of the VSM power shown in Figure 4.27.

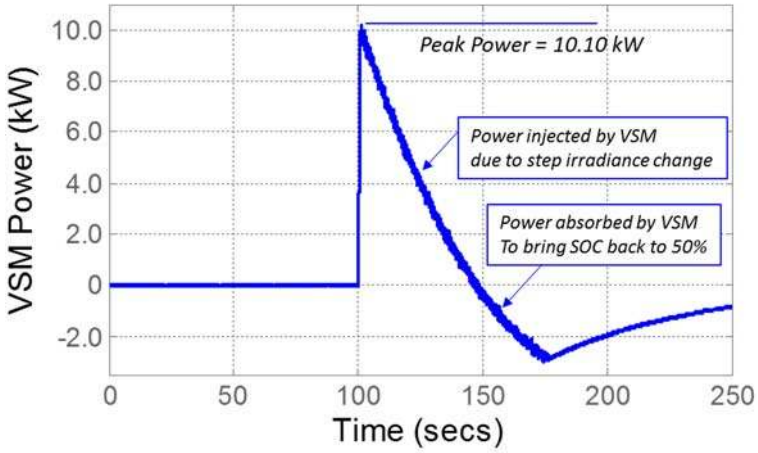

Figure 4.27. Power flow through VSM for step change of irradiance from 750 W/m^2 to 250 W/m^2.

The contribution of the inertial term, the damping term and the state of charge terms to VSM power are shown in Figure 4.28. When there was a drop in the irradiance the VSM provided dynamic frequency support by injecting an inertial peak power of 8.24 kW and a damping peak power of 2.06 kW into the microgrid system. The power injection then gradually lowered as the frequency of the system came back closer to the rated value of 60 Hz. At the same time, since the battery started discharging, the SOC component of the VSM absorbed power from the microgrid system to charge the batteries.

The peak power that the SOC component absorbed was 3.69 kW. As the SOC returned to 50% the absorbed power also decreased gradually.

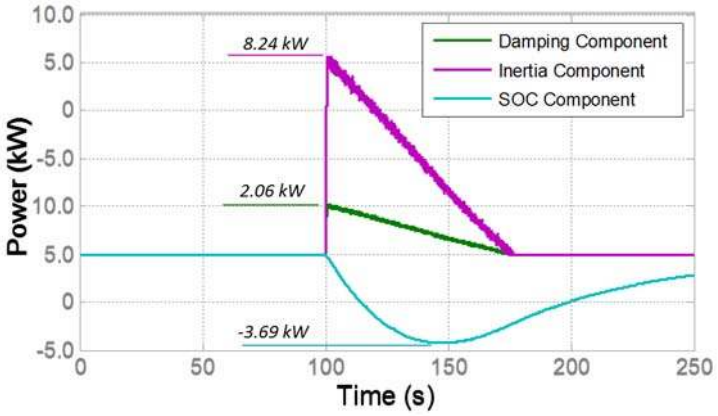

Figure 4.28. Damping and inertial component of power flow through the VSM along with the battery charging/discharging power for step change in irradiance.

Figure 4.29 shows the power that the VSM exchanged with the PV-hydro benchmark system when the real irradiance data described in Section 3.1.3 was used as the input for the PV system. The peak power that the VSM handled in was 12.39 kW which was higher than in case of the step change in irradiance of 750 W/m^2 to 250 W/m^2 (total irradiance change of 500 W/m^2) as described previously. This was because the real irradiance data used had instances of irradiance changes higher than 500 W/m^2 with step irradiance change. The net energy exchange was in fact negative at – 1.11 Wh. In this case the inertial, damping and SOC component of VSM peak power were -2.56 kW, -10.21 kW and 1.94 kW respectively as shown in Figure 4.30.

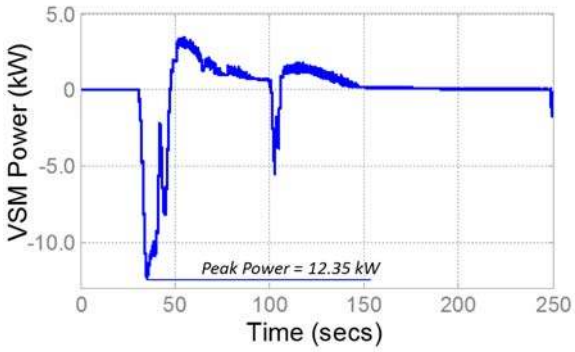

Figure 4.29. Power flow through VSM for real changes in irradiance.

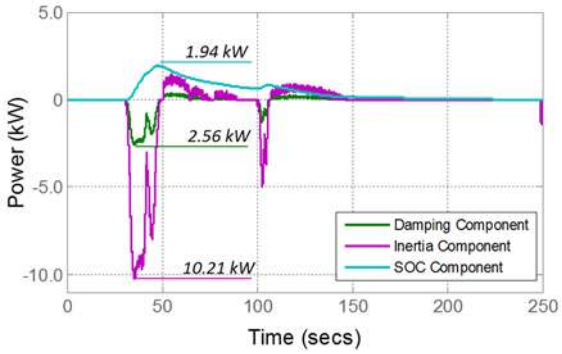

Figure 4.30. Power flow through VSM for real changes in irradiance.

Figure 4.31 shows how the state of charge of the battery changed with and without the SOC control mechanism described in Section 3.3.1. The SOC of battery deviated significantly from the desired 50% value without the SOC control mechanism. But, with the SOC control mechanism the SOC of the battery returned back quickly to 50% and ensured that the VSM was ready for consequent operations.

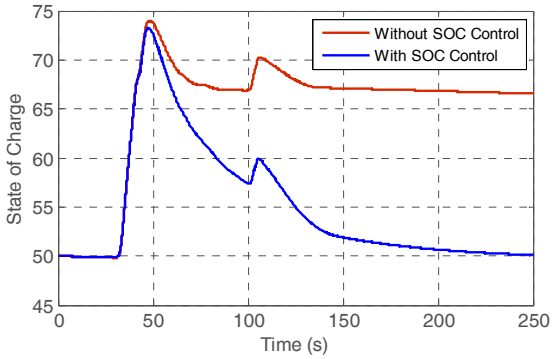

Figure 4.31. State of charge of battery with and without SOC control mechanism.

The net energy exchanged between the VSM and the PV-hydro benchmark system along with the peak power requirements of the VSM's converter for different PV system size of 10 kWp, 15 kWp and 25 kWp are summarized in Table 4.7. In all three cases, the net energy exchange was very low but the peak power requirements of the VSM's converter were significantly high.

Table 4.7. Power flow through VSM for step load change of irradiance from 750 W/m^2 to 250 W/m^2.

PV System Size	Net Energy Exchange	VSM Peak Power
10 kWp	+ 0.04 Wh	4.51 kW
15 kWp	-0.34 Wh	7.19 kW
25 kWp	-1.11 Wh	12.39 kW

Figure 4.32 shows that the peak power handling requirements of VSM increased linearly with the increase in the PV system size. The size of the inverter required was about 50% of the size of the PV system which is quite large compared to the overall system size. The initial investment cost of the inverter for the VSM may limit the

practicability of VSM. But, the peak power requirements of the inverter would drop if the hydro system had a higher inertia constant.

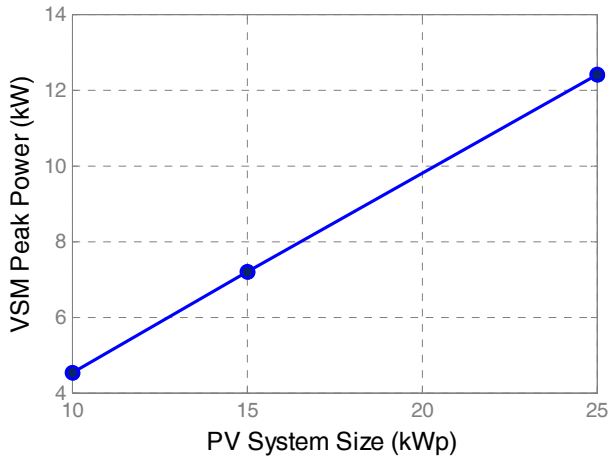

Figure 4.32. PV system size vs VSM peak power.

CHAPTER 5 CONCLUSIONS

5.1. Summary

Photovoltaic-hydro hybrid microgrids can provide reliable clean energy in the remote areas where the electricity grid has not been extended. The inertia of photovoltaic–hydro based microgrid systems is limited to that from the hydro system. Load changes, generation changes and large PV fluctuations can cause large frequency deviations at a large rate of change of frequency. Hence, a dynamic frequency control is required which acts much faster than the primary frequency control (within a few milliseconds) so that it can reduce the high initial rate of change of frequency and keep the system stable. A virtual synchronous machine is a short term energy storage device with power electronics and a dispatching algorithm which makes it behave like a synchronous generator to the grid [4]. It emulates the inertial and damping properties of a real synchronous generator by adding these properties and takes part in the initial inertial response of the system much like a conventional synchronous generator does.

Simulation studies have shown that only 45% photovoltaic penetration can be achieved if the frequency has to be within normal operating frequency range of (± 2%) with system inertia constant of 5 seconds. The penetration was found to reduce dramatically with decreased system inertia constants. The dependence of microgrids on the larger rotational mass of synchronous generators for system inertia was shown. Higher renewable penetration caused large frequency deviations at a high rate of change of frequency which could not be handled by conventional governor control of the synchronous generators. Virtual synchronous machines have been used to improve dynamic frequency control of an autonomous power system consisting of diesel

generators and wind systems. No study has been found on application of virtual synchronous machines to stabilize photovoltaic – hydro microgrid systems. The literature also lacks analysis on potential of increasing photovoltaic penetration in microgrids using a virtual synchronous machine.

A method is needed to improve transient stability for photovoltaic – hydro microgrid systems allowing higher level of photovoltaic penetration. The hypothesis for this study is that if inertia is added to the photovoltaic-hydro microgrid system using a virtual synchronous machine it will maintain and may even improve transient stability. The objective of this thesis was to study the feasibility of using virtual synchronous machines to stabilize photovoltaic-hydro microgrid systems. The specific tasks of this research were to; 1) Study transient stability of photovoltaic – hydro microgrid systems; 2) Study and analyze the use of virtual synchronous machines to reduce frequency variations in photovoltaic– hydro microgrid system and improve its transient stability; and 3) Analyze energy storage requirements for implementation of virtual synchronous machine

A photovoltaic - hydro microgrid is a hybrid system consisting of a hydro generator and a photovoltaic system. Transient stability of a power system is its ability to maintain synchronism when there are instances of severe transient disturbances. The frequency deviations in isolated photovoltaic-hydro systems due to load/generation variations and/or photovoltaic fluctuations may go out of permissible limits. Hence, the transient stability of such systems becomes poor. Modeling and control of three phase voltage source inverters involves use of direct-quadrature axis transformation theory to design voltage and current controllers for the inverter systems. Virtual synchronous machine is an energy storage device with power electronics and a dispatching algorithm

that makes it behave as a synchronous generator for short energy storage requirements. Energy storage systems are used in microgrid stabilization by operating them as spinning reserves to provide power balance between power generation and consumption.

A model of the 39 kW hydro system was developed in MATLAB\Simulink along with the model of a 25 kWp photovoltaic system. The 39 kW hydro system model and the 25 kWp photovoltaic system was connected together to form the photovoltaic – hydro microgrid benchmark model for transient analysis. A three phase current controlled inverter was designed to implement the virtual synchronous machine using direct-quadrature axis based modeling and control techniques. The developed controller was tested in PSIM simulation software. Using the designed current controller designed along with the virtual synchronous machine algorithm the photovoltaic-hydro system with the added virtual synchronous machine was implemented in Opal-RT real time digital simulation software. Software in the loop simulations were performed to perform transient analysis of the photovoltaic-hydro benchmark microgrid with addition of virtual synchronous machine.

Large frequency variations and rate of change of frequency outside the permissible limits, was observed in the photovoltaic-hydro microgrid benchmark system due step irradiance changes and a real irradiance patterns. Simulation results from PSIM shows that the designed current controller operated as designed and the output current of the three phase inverter system could be controlled as reference to the controller changes. Simulation results from the software in the loop simulation performed in Opal-RT, showed that the rate of change of frequency and consequently the frequency variations in the photovoltaic-hydro system was reduced to within permissible limits by emulating

inertia using virtual synchronous machines. The energy requirements were found to be minimal comparable to size of small lead acid or NiMH batteries. The peak power requirements however was up to 50% of the photovoltaic system size.

5.2. Conclusions

The main contribution of this thesis is that it is the first report of using virtual synchronous machines to improve the transient stability of photovoltaic-hydro microgrid systems. It was found that virtual synchronous machines can be used to improve the transient stability of PV-hydro systems and high photovoltaic penetration levels are possible, and the inertial requirements increased linearly with increasing photovoltaic system size. The energy storage requirements of virtual synchronous machines were comparable to the energy capacity of small lead acid or NiMH batteries which indicates the possibility of using short term energy storage technologies like super-capacitors or the capacitance of photovoltaic panels. The peak power requirements of a virtual synchronous machine would be about 50% of the photovoltaic system size that increased linearly with increase in photovoltaic system size. However, if the inertia constant of the hydro system is high the peak power requirements would also drop and reduce the cost of the virtual synchronous machine. This suggests a study is needed to determine if virtual synchronous machine would be cost effective as the cost of the electronics may increase by up to 50%.

5.3. Future Work

Future work should include the implementation of virtual synchronous machine in a real photovoltaic-hydro system to study its performance and cost effectiveness. Also it should be determined if the peak power and the energy storage requirements of the virtual

synchronous machine can be reduced by developing a self-optimizing algorithm. The feasibility of using photovoltaic panels with inherent storage to eliminate the need of dedicated energy storage required for virtual synchronous machine should also be studied.

REFERENCES

[1] A. Gurung, R. Tonkoski, D. Galipeau, and I. Tamrakar, "Feasibility study of photovoltaic-hydropower microgrids," in *5th International Conference on Power and Energy Systems (ICPS),* 2014.

[2] A. Oudalov, D. Chartouni, and C. Ohler, "Optimizing a battery energy storage system for primary frequency control," *Power Systems, IEEE Transactions on,* vol. 22, pp. 1259-1266, 2007.

[3] G. Delille, B. Francois, and G. Malarange, "Dynamic frequency control support by energy storage to reduce the impact of wind and solar generation on isolated power system's inertia," *Sustainable Energy, IEEE Transactions on,* vol. 3, pp. 931-939, 2012.

[4] H. Bevrani, T. Ise, and Y. Miura, "Virtual synchronous generators: A survey and new perspectives," *International Journal of Electrical Power & Energy Systems,* vol. 54, pp. 244-254, 2014.

[5] J. Margeta and Z. Glasnovic, "Introduction of PV energy into an existing HEP," *Energy Conversion, IEEE Transactions on,* vol. 26, pp. 717-727, 2011.

[6] B. E. Türkay and A. Y. Telli, "Economic analysis of standalone and grid connected hybrid energy systems," *Renewable energy,* vol. 36, pp. 1931-1943, 2011.

[7] J. Zhao, K. Graves, C. Wang, G. Liao, and C.-P. Yeh, "A hybrid electric/hydro storage solution for standalone photovoltaic applications in remote areas," in *IEEE Power and Energy Society General Meeting,* 2012, pp. 1-6.

[8] P. Tielens and D. Van Hertem, "Grid inertia and frequency control in power systems with high penetration of renewables," in *Proc. Young Res. Symp. Elect. Power Eng*., pp.1-6, 2012.

[9] A. Ulbig, T. S. Borsche, and G. Andersson, "Impact of low rotational inertia on power system stability and operation," 2013.

[10] M. Torres and L. Lopes, "Frequency control improvement in an autonomous power system: An application of virtual synchronous machines," in *IEEE 8th International Conference on Power Electronics and ECCE Asia (ICPE & ECCE),* pp. 2188-2195, 2011.

[11] H. Beltran, E. Bilbao, E. Belenguer, I. Etxeberria-Otadui, and P. Rodriguez, "Evaluation of storage energy requirements for constant production in PV power plants," *Industrial Electronics, IEEE Transactions on,* vol. 60, pp. 1225-1234, 2013.

[12] Dan Borneo, Matt Lazarewicz, "Energy storage solutions for microgrids.", Clean Energy States Alliance, 2012.

[13] R. Pena-Alzola, R. Sebastian, J. Quesada, and A. Colmenar, "Review of flywheel based energy storage systems," in *International Conference on Power Engineering, Energy and Electrical Drives (POWERENG),* pp. 1-6, 2011.

[14] B. Espinar and D. Mayer, "The role of energy storage for mini-grid stabilization," International Energy Agency, 2011.

[15] S. K. Aditya and D. Das, "Battery energy storage for load frequency control of an interconnected power system," *Electric Power Systems Research,* vol. 58, pp. 179-185, 2001.

[16] D. Kottick, M. Blau, and D. Edelstein, "Battery energy storage for frequency regulation in an island power system," *Energy Conversion, IEEE Transactions on,* vol. 8, pp. 455-459, 1993.

[17] H. P. Beck and R. Hesse, "Virtual synchronous machine," in *9th International Conference on Electrical Power Quality and Utilisation*, pp. 1-6, 2007.

[18] R. Hesse, D. Turschner, and H.-P. Beck, "Micro grid stabilization using the Virtual Synchronous Machine (VISMA)," in *International Conference on Renewable Energies and Power Quality, Barcelona,* 2009.

[19] K. Visscher and S. De Haan, "Virtual synchronous machines (VSG's) for frequency stabilisation in future grids with a significant share of decentralized generation," in *Proc. IET-CIRED Semin. Smart-Grids Distrib,* pp. 1-4, 2008.

[20] K. Sakimoto, Y. Miura, and T. Ise, "Stabilization of a power system with a distributed generator by a Virtual Synchronous Generator function," in *IEEE 8th International Conference on Power Electronics and ECCE Asia (ICPE & ECCE),* pp. 1498-1505, 2011.

[21] N. Soni, S. Doolla, and M. C. Chandorkar, "Improvement of transient response in microgrids using virtual inertia," *Power Delivery, IEEE Transactions on,* vol. 28, pp. 1830-1838, 2013.

[22] V. Karapanos, S. de Haan, and K. Zwetsloot, "Testing a virtual synchronous generator in a real time simulated power system," in *Proc. Int. Conf. on Power Systems Transients (IPST)*, 2011.

[23] M. Torres and L. A. Lopes, "Virtual Synchronous Generator: A control strategy to improve dynamic frequency control in autonomous power systems," *Energy and Power Engineering,* vol. 5, pp. 32, 2013.

[24] P. Kundur, *Power system stability and control*, 9th Edition ed.: Tata McGraw-Hill, 2010.

[25] R. A. Messenger, J. Ventre, *Photovoltaic system engineering*, 3rd Edition ed.: CRC Press, 2010.

[26] Myelectrical.com, "My Electrical", 2015. [Online]. Available: http://myelectrical.com/. [Accessed: 15- Apr- 2015].

[27] Solarprofessional.com, "Field applications for I-V curve tracer", 2015. [Online]. Available: http://www.solarprofessional.com. [Accessed: 21-Apr-2015].

[28] G. Andersson, *Dynamics and control of electric power systems*, Lecture notes-Swiss Federal Insititute of Technology, 2012.

[29] M. H. Rashid, *Power electronics handbook: devices, circuits and applications*, 2nd Edition ed.: Prentice Hall of India, 1996.

[30] N. Mohan, T. M. Undeland, W.P. Robbins, *Power electronics: converters, applications, and design,* 3rd Edition ed.: Wiley India, 2010.

[31] W. Duesterhoeft, M. W. Schulz, and E. Clarke, "Determination of instantaneous currents and voltages by means of Alpha, Beta, and Zero components," *American Institute of Electrical Engineers, Transactions of the,* pp. 1248-1255, 1951.

[32] "MATLAB/Simulink documentation ," Version 2011b ed: Mathworks, 2011.

[33] R. H. Park, "Two-reaction theory of synchronous machines generalized method of analysis-part I," *American Institute of Electrical Engineers, Transactions of the,* vol. 48, pp. 716-727, 1929.

[34] M. P. N. van Wesenbeeck, S. W. H. de Haan, P. Varela, and K. Visscher, "Grid tied converter with virtual kinetic storage," in *IEEE PowerTech, Bucharest*, pp. 1-7, 2009.

[35] Y. Chen, R. Hesse, D. Turschner, and H.-P. Beck, "Improving the grid power quality using virtual synchronous machines," in *International conference on Power engineering, energy and electrical drives (POWERENG),* pp. 1-6, 2011.

[36] Y. Bhandari, "Fuel reduction in remote microgrids using photovoltaics, battery and multiple generators," M.S. Thesis, Department of Electrical Engineering and Computer Science, South Dakota State University, Brookings, SD, USA, 2013.

[37] R. C. Dorf and R. H. Bishop, "Modern control systems," 10th Edition ed.: Pearson, 2010.

[38] R. Tonkoski, *Computer aided analysis of power electronic systems,* Lecture Notes, South Dakota State University, 2015.

[39] "Reciprocating internal combustion engine driven alternating current generating sets," in *Generating Sets (ISO 8528-5)*, ed: ISO, 2005.

[40] B. Liu, D. Thomas, K. Jia, and M. Woolfson, "Advanced ROCOF protection of synchronous generator," in *IEEE PES Innovative Smart Grid Technologies (ISGT),* pp. 1-6, 2011.